# The Nanotech France 2024 International Conference

## June 05 to 07 2024
## Conference Proceedings

# A Novel Memristor Design based on Hydrogen Movement on Silicon Surfaces

Naznin Nahar Nipu[1], Peter J. Schubert[1]

[1] Indiana University-Purdue University Indianapolis
Indianapolis, Indiana, USA, nnipu@iu.edu, pjschube@iu.edu

## Abstract

As edge computing advances, memristors are needed for enhanced performance and scalability with minimal energy, but precise resistance switching is a challenge. Silicon (Si) surfaces in a proton-conducting polymer can control memristor behaviour by depositing hydrogen (H) atoms, which increase conductivity via mid-gap traps, forming a memristor unit cell. This study investigates the critical function of H atoms by deliberately altering their positioning and concentration in silicon-based memristor devices. Using the Large-scale Atomic/Molecular Massively Parallel Simulator (LAMMPS), we investigate the impact of temperature (T) and electric field (EF) on H migration. We define a polygonal volume of Si and deposit H atoms on its top surface. We apply T and EF to observe diffusion and drift of H atoms. The hopping rate depends on applied T and EF. We establish a relationship between the three-dimensional velocity of H and applied T and EF. We simulate several movement pathways of H atoms over time under varying T and EF acting separately or simultaneously. Therefore, we can determine the required magnitude and direction of EF and T to achieve the desired H position and concentration. Our approach aims to improve edge computing and neuromorphic computing by enhancing memristor functionality. Despite potential scalability issues and the need for precise hydrogen control, this research offers valuable insights into modifying memristor electrical characteristics for low-energy silicon-based neuromorphic devices.

**Keywords:** hydrogen migration, LAMMPS, memristive properties, resistance manipulation, edge computing, neuromorphic computing

## 1. Introduction

Efficient and accurate computing chips are crucial for modern technology, especially with the increasing data demands of AI applications [1]. While the von Neumann architecture faces high power and heat challenges [2], the memristor offers a potential solution by integrating memory and computing functions in a single framework [3]. Memristor is a two terminal device and involves sandwiching one or multiple thin layers of memristive material between two metal electrodes. Memristors can switch between high and low resistance state depending on the applied voltage [4]. Traditionally, metal oxide memristive materials are used, although oxide ions and vacancies move slowly and can negatively impact the conductivity modulation process [5]. Silicon (Si)-based memristors offer several advantages, including compatibility with existing CMOS technology and fast switching speed [6]. Hydrogen (H) can be used as a dopant to modify the electrical properties of Si, allowing for control over its conductivity [7]. Additionally, it makes defect engineering possible, allowing charge carriers to be trapped in critical ways [8] that ease transitioning between high and low conductivity states. Considering these advantages, we are proposing a Si based memristor with a polyaniline (PA) layer on top of it. PA is a proton-conducting polymer such that one can move H atoms between PA and Si layers. This study uses molecular dynamics simulations to investigate how temperature variations and electric fields affect hydrogen migration and memristor behaviour, particularly for neuromorphic applications.

## 2. Methods

### 2.1. Simulation Setup

We used the Big Red 200 [9], an HPE Cray EX supercomputer provided by Indiana University for this study. The simulations were performed by the LAMMPS software [10]. Data generated by LAMMPS were post-processed by MATLAB for further analysis. We defined a 3-dimensional system with "real" units and free boundary conditions. A diamond lattice for Si atoms with a lattice constant of 5.4307 Å was used, creating a simulation box of dimensions [70.5991; 38.0149; 38.0149] Å. The box contained 1638 Si atoms with 7 H atoms deposited on the surface. We used the "ReaxFF" reactive force field and the "NVE" ensemble, with temperature

($T$) control via the Langevin thermostat and a timestep of 0.05 fs. Output files recorded Si-H bond information, while LAMMPS trajectory files tracked each atom's partial charge ($q$), position ($x, y, z$), kinetic energy ($KE$), and velocity ($v$). To study H atom relocation, we applied a bias voltage as an EF, setting velocities and forces to zero to isolate the field's effects.

## 2.2. Temperature and Electric Field-Dependent Hydrogen Movement on Silicon Surfaces

We simulated H atom diffusion on Si surfaces at 70 K, 180 K, 280 K, 380 K, and 480 K without an EF. We then applied *EF* of 0.000003, 0.00001, 0.00003, 0.0001, and 0.0003 V/Å along the +x direction, keeping the $T$ constant. Post-processing yielded *KE* and *v* over time. Data regression determined the relationship between H atom's *v, T, t,* and *EF*. These were used to estimate H atom's movement pathways under various conditions and were analysed to assess impacts on device performance.

## 3. Results

Fig. 1(a) demonstrates the *KE* distribution of H atom number 1641 at 480 K along with theoretical M-B distribution for validation. It is evident that *KE* rises with temperature fluctuating arbitrarily between 0 and 0.07 eV at 70 K whereas the upper boundary increased to 0.4 eV at 480 K. *KE* of H atoms changes randomly in different directions at a vibrational frequency of $1.54 \times 10^{13}$ s$^{-1}$ [11]. Most of these kinetic energies cannot surmount the bond energy barrier of 1.2 eV and contribute to hopping of H atoms by moving ~2.5 Å from one Si to the neighbouring Si. To estimate the *v* that can cause H migration we used the M-B distribution and calculated the probability that *KE* of H atom is higher than 1.2 eV. Hop rate equals to the product of vibrational frequency and probability ($KE > 1.2$ eV). Therefore, the velocity can be calculated by taking the product of hop rate and distance between two Si atoms. After calculating *v* at different *T*, we applied regression method as shown by Fig. 2(a) and found the following relation between *v* and *T*.

$$v_T = 13100 \, e^{-13820\left(\frac{1}{T}\right)}$$

It is observed that, at a given *EF*, velocity of a hydrogen atom increases linearly over time. A higher *EF* makes the acceleration of the atoms faster as shown by Fig. 2(b). The relation between v, *EF,* and time *t* can be expressed as,

$$v_{EF} = 1.3 \times 10^{-5} \times EF \times t$$

Here *v* is measured in Å/fs, *T* is measured in K, *EF* is measured in V/ Å, and *t* is measured in fs. Combined velocity due to the simultaneous effect of *T* and *EF* can be expressed as,

$$v_C = v_T + v_{EF}$$

Considering the position of hydrogen atom at time $t$ is $P_t$, we can use the following equation to calculate the next position after a short time interval $\Delta t$:

$$P_{t+\Delta t} = P_t + v_C \, \Delta t$$

We developed a MATLAB program to track H atom's migration on Si surfaces. Without an *EF*, H atoms moved randomly due to *T*, with no hopping observed. When both *T* and *EF* were applied, *EF* directed H atoms in the direction of the applied field, while *T* introduced randomness. Initially, diffusion dominates, but over time, *EF*'s influence grew, causing H atoms to accelerate in the *EF* direction. An initial bias places H atoms to form a conductive channel, ensuring state retention after bias removal. Memristors can face varying *T* disrupting H placement and conductivity. In such cases, a bias can realign the atoms. High *T* might also serve as an "erase" function for repurposing the memristor. Consider the length and width of the Si structure is 10 microns, and the thickness of the PA film is 1 micron. Fig. 4(a) illustrates that at 380 K, with an electric field as low as $10^{-30}$ V/Å, it takes almost $8.77 \times 10^4$ s (~24 hours) to change the conductivity from 100% to 0% whereas at higher electric field of $10^{-3}$ V/Å it only takes 2.77 ns. To investigate the influence of *T*, 50% diffusion is taken as the point at which the memristor device's original function degrades to an unreliable level. At 100 K it would take ~$1.27 \times 10^{38}$ years for the device to lose its 50% memory (i.e. "never"). At 300 K (room *T*) it would takes just 4.5 days, whereas at 400 K only 3.85 seconds. This study can tell how long it takes to "erase" or randomize the configuration of H atoms to return the memristor into the uniform H layer having the highest conductivity.
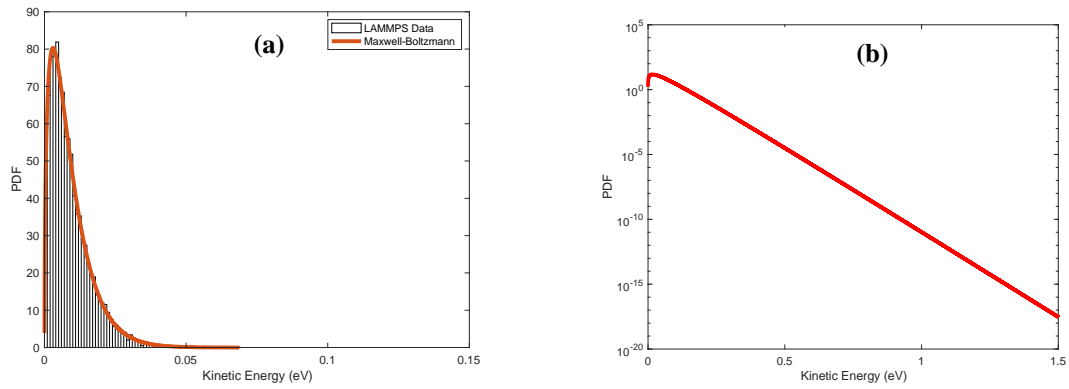
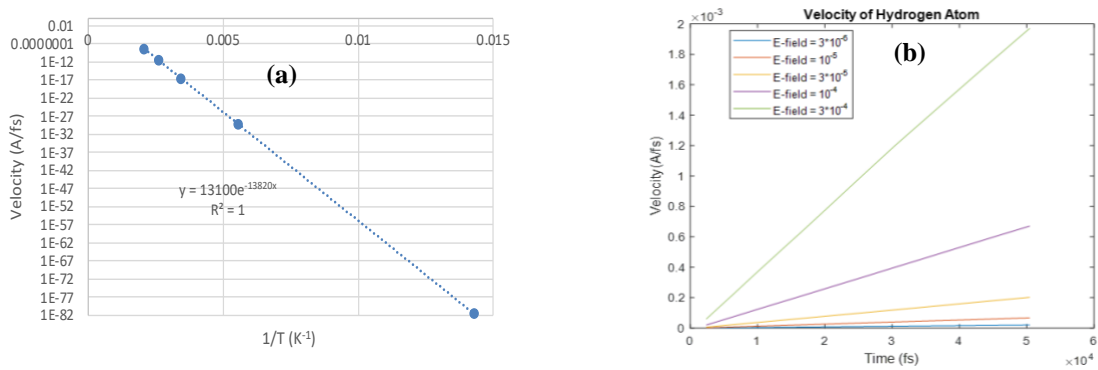**Fig. 1**: (a) KE distribution of H atom 1641 at 480 K with M-B distribution at linear scale, (b) log scale.



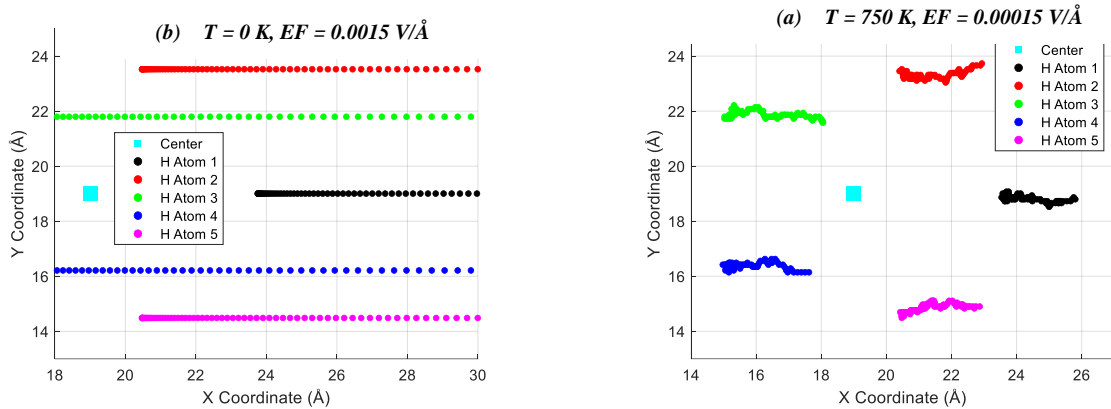**Fig. 2**: (a) Relation between *v* and *T*, (b) relation between *v, EF,* and *t*



**Fig. 3**: H atom movement due to (a) drift only, (b) combined effect of drift and diffusion.
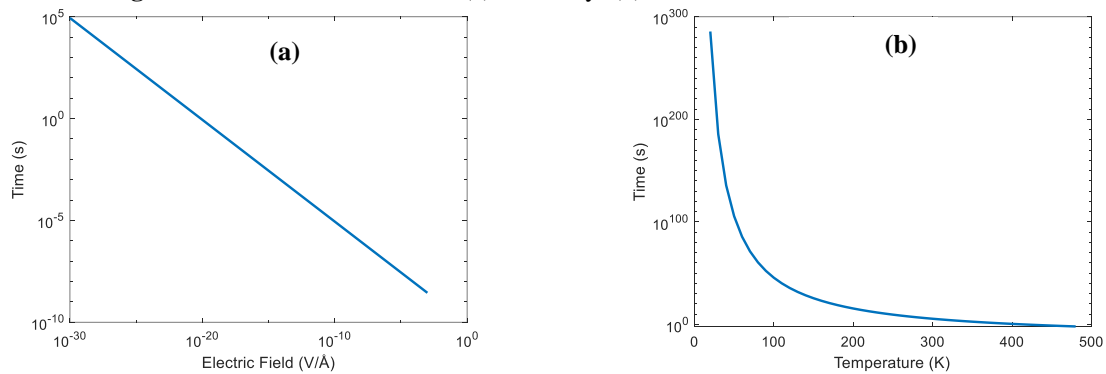


**Fig. 4**: Time to drop H atom conductivity (a) from 100% to 0% at various EF; (b) from 100% to 50% at various T.

## 4. Discussion and Future Work

We proposed a Si-based memristor with a PA top layer, featuring 3-D conductivity modulation via three pairs of electrodes. H atoms, introduced into the PA layer using a catalyst like palladium, migrate to the Si layer

under a bias voltage, modulating conductivity and memory retention. Using molecular dynamics, we studied the impact of *T* and *EF* on H movement on the Si surface, validated against the M-B distribution. We found that T disperses H atoms, increasing entropy and affecting memory state, while *EF* cause H drift. The interplay between *T* and *EF* influences H atom diffusion and drift, with higher *T* favouring diffusion and higher *EF* favouring drift. This can reset the memristor or modify its conductivity. We developed a mathematical relationship to predict H velocity and migration, informing circuit design and operating conditions for pre-programming, gradual conductivity changes (neuroplasticity), and reset functions in memristor devices and arrays. This work is an important first step in modelling a novel neuromorphic device based on H movement across porous silicon. Future studies should investigate hydrogen migration in larger systems and different crystal surfaces, use "ab initio" tools and scanning tunnelling microscopy and validate computational results with laboratory experiments. Assessing the long-term stability and programming cycle limits of the memristor device will ensure its reliability and functionality over extended use.

## Acknowledgements

## References

1. Chen, C., & Zhang, C.-Y. (2014). Data-intensive applications, challenges, techniques and technologies: A survey on Big Data. *Information Sciences*, *275*, 314–347. https://doi.org/10.1016/j.ins.2014.01.015
2. G. E. Hinton and R. R. Salakhutdinov, "Reducing the dimensionality of data with neural networks," *Science*, vol. 313, no. 5786, pp. 504-507, 2006. doi: 10.1126/science.1127647.
3. Q. Chen, T. Han, M. Tang, Z. Zhang, X. Zheng, and G. Liu, "Improving the recognition accuracy of memristive neural networks via homogenized analog type conductance quantization," *Micromachines*, vol. 11, no. 4, pp. 427, 2020. doi: 10.3390/mi11040427.
4. Luo, L., Dong, Z., Duan, S., & Lai, C. S. (2020). Memristor-based stateful logic gates for multi-functional logic circuit. *IET Circuits, Devices & Systems*, *14*. https://doi.org/10.1049/iet-cds.2019.0422.
5. X. Shan et al., "Plasmonic optoelectronic memristor enabling fully light-modulated synaptic plasticity for neuromorphic vision," *Adv. Sci.*, vol. 9, no. 6, p. 2104632, 2022. doi: 10.1002/advs.202104632.
6. Y.-F. J. Chang et al., "Intrinsic SiOx-based unipolar resistive switching memory. I. Oxide stoichiometry effects on reversible switching and program window optimization," *J. Appl. Phys.*, vol. 116, no. 4, p. 043708, 2014. doi: 10.1063/1.4891242.
7. O. Sikder and P. Schubert, "A Theoretical Study on Porous-Silicon Based Synapse Design for Neural Hardware," in *2021 IEEE 16th Nanotechnology Materials and Devices Conference (NMDC)*, 2021, pp. 1-4. doi: 10.1109/NMDC50713.2021.9677557.
8. M. A. Haque et al., "Role of Dopants in Organic and Halide Perovskite Energy Conversion Devices," *Chem. Mater.*, vol. 33, no. 21, pp. 8147-8172, 2021. doi: 10.1021/acs.chemmater.1c01867.
9. "Supercomputers for academic research at IU," accessed May 12, 2024, [Online]. Available: https://kb.iu.edu/d/alde
10. A. P. Thompson *et al.*, "LAMMPS - a flexible simulation tool for particle-based materials modeling at the atomic, meso, and continuum scales," *Computer Physics Communications*, vol. 271, p. 108171, Feb. 2022, doi: 10.1016/j.cpc.2021.108171.
11. M. Boaks and P. Schubert, "Kinetics of hydrogen storage on catalytically-modified porous silicon," Journal of Catalysis, vol. 371, pp. 81–87, 2019. https://doi.org/10.1016/j.jcat.2019.01.033

# Low temperature synthesis of crystalline GaN from a mixture of Li and Ga under $N_2$ atmosphere

Youting Song

Beijing National Laboratory for Condensed Matter Physics, Institute of Physics, Chinese Academy of Sciences, Beijing, People's Republic of China, ytsong@iphy.ac.cn

## Abstract

GaN has been synthesized by using Li/Ga mixture as starting materials at 340-575℃ and 1-2 atm of $N_2$, and characterized by XRD, SEM, Raman spectra, and PL spectra, which shows that GaN synthesized at 340℃ is in nano-sized; GaN synthesized below 510℃ and with a holding time of 12-48h is of high purity and highly crystalline. Meanwhile, the formation mechanism of GaN was investigated. Li first reacts with $N_2$ to produce $Li_3N$, and then Ga combines simultaneously with Li and N in $Li_3N$ to produce GaN and LiGa, and the formation of by-product LiGa makes Gibbs free energy of the reaction ($Li_3N + Ga = GaN + GaLi$) negative, and thus plays a key role to the synthesis of GaN. In addition, the releasing heat in the nitriding process of Li raises the temperature of the whole system, and thus enhances the reaction rate of $Li_3N$ and Ga. So, the synthesis of crystalline GaN embodies the double contributions from kinetics and thermodynamics of whole system.

**Keywords**: crystalline GaN, formation mechanism of GaN, XRD, SEM, Raman spectra, and PL spectra, wide bandgap semiconductor.

## 1. Introduction

Gallium nitride (GaN) is a direct and wide bandgap semiconductor commonly used in short wavelength optoelectronics and high-power and high-frequency electronics [1-3]. Due to the lack of bulk GaN crystals, Ⅲ-nitride-based devices are mainly fabricated on foreign substrates like sapphire, SiC, Si [4-5]. The lattice mismatch and thermal expansion coefficient difference between GaN films and foreign substrates lead to nitride epilayer with high stress and high dislocation density, and thus deteriorate the performances of these devices. Therefore, developing bulk GaN crystal with high quality is urgent. GaN bulk crystals can be prepared by several techniques including hydride vapor phase epitaxy (HVPE) [6], ammonothermal [7], alkali metal flux [8-12], high pressure solution growth [13] and sublimation method [14]. At present, 2-inch GaN wafers are commercially available for HVPE by means of a two-step reaction, but the wafers acquired by this method still suffers from disadvantage of large dislocation density ($>10^6/cm^2$) [6]. 2-inch GaN wafers can be also obtained through the ammonothermal, and Na-flux method, especially for ammonothermal method, as an analog of hydrothermal one, it possesses good scalability, and the dislocation density of GaN wafers prepared by this method is two orders of magnitude lower than that of HVPE [7], which is advantageous especially for the application in blue laser diodes and electronics. In addition, employing high pressure solution technique, the dislocation density of GaN crystal can reach $10^2/cm^2$, but its growth conditions (1Gpa and 1500℃) are so harsh that it is difficult to further enlarge the size of growth chamber and achieve mass production of GaN wafers.

Polycrystalline GaN can be used for source material to prepare GaN crystals by sublimation method, and usually synthesized by the reaction of metal Ga (or gallium oxide) and $NH_3$ at T>900℃[15-16]. Using Li as a nitrogen fixant, crystalline GaN can be synthesized under flowing ammonia [17-18]. Moreover, the synthesis of the crystalline GaN can be completed from solid precursors at atmosphere pressure [19]. But all these methods use a toxic gas -ammonia as a resource material, therefore environmental pollution is inevitable.
Here, we report the synthesis of crystalline GaN by a physical mixture of Li/Ga at 415-575℃ and under 1-2atm $N_2$ and propose a formation mechanism of GaN based on experimental results and thermodynamic calculation.

## 2. Experiment

A mixture of metal Li and Ga was used as starting materials for the synthesis of GaN. Liquid Ga and Li ribbon with a proper molar ratio were weighed and loaded into a tungsten crucible (20mm inner diameter,

20mm depth). The crucible was placed in a stainless steel furnace by induction heating. Before reaction, the furnace was first evacuated down to $3.0 \times 10^{-3}$ Pa, and then filled with 1-2 atm of $N_2$ (flowing $N_2$ or non-flowing). The crucible was heated to 300-600℃ with a rate of 3-5℃/min, and held there for 12-72 h, and then cooled to room temperature within 4h. The crucible was taken out from the furnace and then the product was repeatedly washed by a dilute HCl solution and then de-ionized water. Finally, crystalline GaN is obtained and characterized by XRD, SEM, Raman, and PL spectra.

## 3. Result and Discussion

The experimental results under various conditions are listed in Table 1. From table 1 it can be found that GaN can be obtained at temperatures ranging from 340°C to 575°C, but only nano-sized GaN particles can be synthesized at 340°C, while crystalline GaN with micro-meter sizes can be synthesized at 415-575°C, and the crystalline GaN exhibits hexagonal shape with well-defined edges (figure1). Figure 2 shows X-ray powder diffraction patterns of GaN prepared at different temperatures and it can be observed that the diffraction peaks of these particles prepared at 340℃ become broadening for its nanometer size effect [20] ; the diffraction peaks at 415-575°C is sharp, indicating that these particles are highly crystalline. In the experiments we also find that the purity of the final products is in relation to holding time and the experimental temperatures. When holding times are between 12-48h and the experimental temperature is below 510°C, highly pure GaN can be obtained; while holding time is 72h, some impurity (its diffraction peak: 21.27°, 39.75 °) always appears in the final products (figure 2), and when the experimental temperature reaches 575°C, some new diffraction peaks (22.58°, 26.50°, 26.92°, 30.20°, 30.49°, 39.27°, 39.55°, 40.51°, 41.47°, 41.67°, 42.03°) corresponding to another impurity are observed, according to retrieving result with ICDD database, those two impurities are identified as $Li_2WO_4$ and $Li_2W_2O_7$, respectively. We infer that lithium metal reacts with tungsten crucible in the nitrogen ambient to yield lithium tungsten nitride, and the result of the hydrolysis of lithium tungsten nitride when the reaction products are washed by water. In addition, in the  preparation of GaN whether the nitrogen flows or not has little effect on the experimental results, and the proper mole ratios of Li/Ga are between 3 and 7.

Table 1: The Results under different experimental conditions

| Li/Ga mole ratio | Temperature (℃) | Hold Time (h) | $N_2$ Pressure (atm) | Final Products | Products Containing Impurity, or not |
|---|---|---|---|---|---|
| 1:7 | 340 | 72 | 1.25 (flowing $N_2$) | Nano-sized GaN | yes |
| 1:7 | 415 | 72 | 1.25 (flowing $N_2$) | Crystalline GaN | yes |
| 1:7 | 465 | 72 | 1.25 (flowing $N_2$) | Crystalline GaN | yes |
| 1:7 | 575 | 72 | 1.25 (flowing $N_2$) | Crystalline GaN | yes |
| 1:3.5 | 510 | 48 | 1.25 (flowing $N_2$) | Crystalline GaN | no |
| 1:1 | 465 | 24 | 1.25 (non-flowing) | Crystalline GaN | no |
| 1:1 | 465 | 48 | 1.25 (non-flowing) | Crystalline GaN | no |
| 1:10 | 465 | 48 | 1.25 (non-flowing) | Crystalline GaN | no |
| 1:3.5 | 465 | 12 | 1.25 (non-flowing) | Crystalline GaN | no |
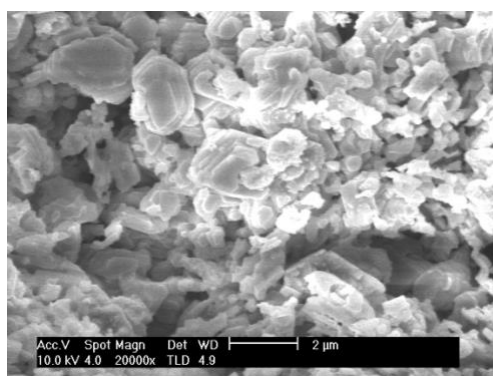


**Fig. 1**: A scanning electron micrograph of crystalline GaN prepared at 510°C. Image shows the well-defined hexagonal features of crystalline GaN
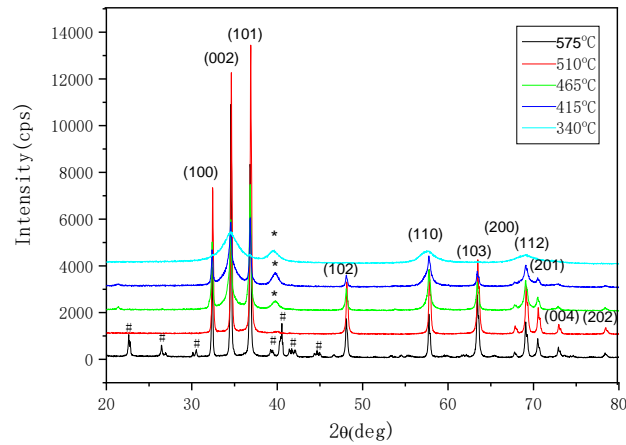
**Fig. 2**: X-ray powder diffraction patterns of GaN prepared at different temperatures. Hold 48h at 510℃; hold 72h at other temperatures. Peaks represented by symbol * and # show diffraction peaks from impurities.

At next part, we shall give the reaction mechanism according to experimental results and theoretical calculation. When Li and Ga are used for the starting materials, because the reaction of Li and $N_2$ can occurs at low temperature, even room temperature, Li first reacts with $N_2$ to generate $Li_3N$, and then $Li_3N$ react with Ga to form GaN. However, it has been reported that the reaction ($Li_3N+Ga=GaN+3Li$) is not thermodynamically favoured [21-22], therefore, we infer that another product of the reaction should be GaLi, $Ga_2Li_3$, $GaLi_2$, not Li. According to thermodynamic data reported [23-27] we calculate $\Delta G^o$ of the reaction: $Li_3N + Ga \rightarrow GaN + 3Li$, at 415℃, 750℃, respectively.

$\Delta G^o = G^o_{GaN} + 3G^o_{Li} - G^o_{Li3N} - G^o_{Ga} = 65.19 \text{kcal/mol} (415℃)$
$\Delta G^o = G^o_{GaN} + 3G^o_{Li} - G^o_{Li3N} - G^o_{Ga} = 3.45 \text{kcal/mol} (750℃)$

Their $\Delta G^o > 0$, meaning that the reaction ($Li_3N + Ga \rightarrow GaN + 3Li$) at 415-750℃ cannot spontaneously occur. To further confirm our conjecture, we also calculate $\Delta G^o$ of the following several reactions:

$Li_3N + 4Ga \rightarrow GaN + 3GaLi$ (1).
$\Delta G^o = G^o_{GaN} + 3G^o_{GaLi} - G^o_{Li3N} - G^o_{Ga} = -121.64 \text{kcal/mol} (415℃)$
$\Delta G^o = G^o_{GaN} + 3G^o_{GaLi} - G^o_{Li3N} - G^o_{Ga} = -72.07 \text{kcal/mol} (750℃)$
$Li_3N + 3Ga = GaN + Li_3Ga_2$ (2)
$\Delta G^o = G^o_{GaN} + 3G^o_{Ga2Li3} - G^o_{Li3N} - G^o_{Ga} = -141.89 \text{kcal/mol} < 0 (415℃)$
$2Li_3N + 5Ga = 2GaN + 3GaLi_2$ (3)
$\Delta G^o = 2G^o_{GaN} + 3G^o_{GaLi2} - 2G^o_{Li3N} - 5G^o_{Ga} = -241.86 \text{kcal/mol} < 0 (415℃)$

Their $\Delta G^o < 0$, meaning that these reactions can spontaneously occur, as presented by the experiments. Therefore, the formation of LiGa, $Li_3Ga_2$, $Li_2Ga$ makes Gibbs free energy of the whole reaction negative, and thus plays a key role in the synthesis of GaN. Here, taking LiGa (one of the products) as an example, the whole reaction process is given as follows

$Li + N_2 \rightarrow Li_3N$ (4)

$$Li_3N + 4Ga \rightarrow \begin{matrix} Ga \\ \backslash \\ Li \\ \backslash \\ Ga - - - Li - N - - Ga \\ \diagup \\ Li \\ \diagup \\ Ga \end{matrix} \rightarrow GaN + 3GaLi \quad (5)$$
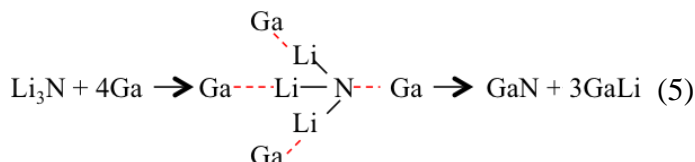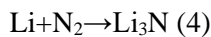
From the above calculation result, $\Delta G^o$ at 415℃ is more negative than that at 750℃, which means that the reaction is easier to occur at lower temperatures, but because of the limitation in kinetics, the reaction rate is larger at the higher temperature. Actually, the temperature of gallium nitride synthesis with lithium nitride and gallium as raw materials should be above 700℃ [9], and why gallium nitride can be synthesized in the temperature range of 340-575℃ under nitrogen atmosphere with lithium/gallium mixture as raw materials is

due to the fact that the nitriding of Li to form lithium nitride releases a large amount of heat, which increases the temperature of the whole system and accelerates the reaction rate of lithium nitride and gallium. Therefore, here the forming reaction of GaN reflects dual contributions in both kinetics and thermodynamics. When GaLi alloy is used as a crude material no GaN was formed under same conditions, for GaLi alloy is stable, breaking triple bonds in $N_2$ is difficult, the possibility to yield GaN by the reaction of GaLi with $N_2$ is small, which means that $Li_3N$ at current conditions is indispensable to get GaN.
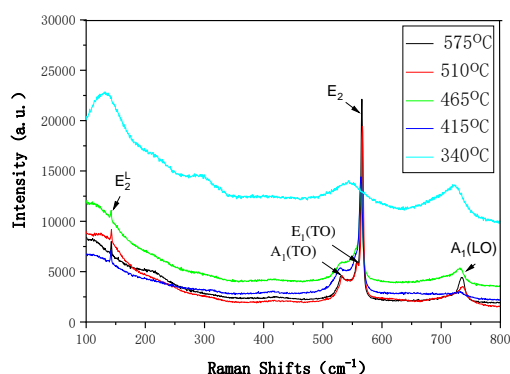


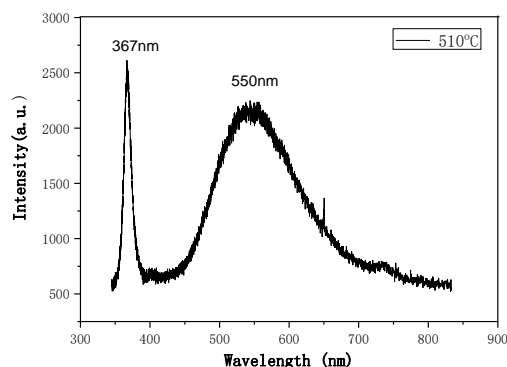**Fig. 3**: Raman scatering spectra of GaN



**Fig. 4**: Room-temperature photoluminescence spectrum of crystalline GaN excited at 325nm.

Figure 3 presents the Raman scattering spectra of GaN synthesized at different temperatures. It has been reported that bulk GaN has six first-order Raman active phonons, namely A1(TO), A1(LO), E1(TO), E1(LO), E2 (high), and E2(low), with frequencies at 533, 735, 561, 743, 569, and 144 cm$^{-1}$, respectively [28]. The bands at 531, 734, 558, 566, and 142 cm$^{-1}$ for our crystalline GaN prepared at temperature 415-575°C can be attributed to A1(TO), E1(TO), E1(TO), E2(high), and E2 (low) modes of hexagonal GaN, respectively. However, the bands at 722, 544 and 130 cm$^{-1}$ of GaN prepared at temperature 340°C are broadened and shift toward lower frequency. In addition, one additional band at 293 cm$^{-1}$ is also observed, probably resulted from defects [29].

A typical room-temperature PL spectrum of the crystalline GaN excited at 325 nm is shown in Figure 4. The PL spectrum of the crystalline GaN shows a strong band edge emission and a well-known yellow luminescence (YL) band centred at 550nm is observed [30].

## 4. Conclusion

GaN has been synthesized by using Li/Ga mixture as starting materials at 340-575℃ and 1-2 atm of $N_2$, and characterized by XRD, SEM, Raman spectra, and PL spectra, which presents that GaN synthesized at 340℃ is in nano-sized; GaN synthesized below 510℃ and with a holding time of 12-48h is of high purity and highly crystalline. The formation mechanism of GaN was suggested as follows: Li first reacts with $N_2$ to produce $Li_3N$, and then Ga combines simultaneously with Li and N in $Li_3N$ to produce GaN and GaLi ($Ga_2Li_3$, $GaLi_2$), and the formation of by-product (GaLi, $Ga_2Li_3$, $GaLi_2$) makes Gibbs free energy of the whole reactions negative, as a result the chemical reaction proceeds spontaneously in forward direction. In addition, the releasing heat in the nitriding process of lithium raises the temperature of the whole system, and thus enhances the reaction rate of $Li_3N$ and Ga. Thus, the synthesis of crystalline GaN embodies the dual contributions from kinetics and thermodynamics of whole system.

## 5. Acknowledgement

## References

1.   S. Nakamura, T. Mukai, and M. Senoh, "Candela-class high-brightness InGaN/AlGaN double-heterostructure blue-light-emitting diodes"，Applied Physics Letters, vol. 64, pp.1687-1689, 1994..

2. S. Nakamura, M. Senoh, S. I. Nagahama, N. Iwasa, T. Yamada, T. Matsushita, H. Kiyoku and Y. Sugimoto, "InGaN-Based Multi-Quantum-Well-Structure Laser Diodes", Jpn. J. Appl. Phys. Vol.35, pp.L74-L76, 1996.

3. H. Okumura, "Present status and future prospect of wide gap semiconductor high-power devices", Japanese Journal of Applied Physics, vol. 45 no.10A, pp.7565-7586, 2006.

4. L. Liu, J. H. Edgar, "Substrates for gallium nitride epitaxy"，Materials Science and Engineering R, vol.37, pp.61-127, 2002.

5. D. G. Zhao, S. J. Xu, M. H. Xie, and S. Y. Tong, "Stress and its effect on optical properties of GaN epilayers grown on Si(111), 6H-SiC(0001), and c-plane sapphire", Applied Physics Letters, vol.83, pp.677-679, 2003.

6. M. K. Kelly, R. P. Vaudo, V. M. Phanse, L. Gorgens, O. Ambacher and M. Stutzmann, "Large free-standing GaN substrates by hydride vapor phase epitaxy and laser-induced liftoff", Jpn. J. Appl. Phys. vol.38, pp.L 217-L 219, 1999.

7. R. Dwilinski, R. Doradzinski, J. Garczynski, L. Sierzputowski, R. Kucharski, M. Zajac, M. Rudzinski, R. Kudrawiec, J. Serafinczuk, W. Strupinski, "Recent achievements in ammono-bulk method", Journal of Crystal Growth, vol. 312, pp. 2499-2502, 2010.

8. F. Kawamura, M. Morishita, M. Tanpo, M. Imade, M. Yoshimura, Y. Kitaoka, Y. Mori, T. Sasaki, "Effect of carbon additive on increases in the growth rate of 2 in GaN single crystals in the Na flux method", Journal of Crystal Growth, vol.310, pp.3946– 3949, 2008.

9. Y. T. Song, W. J. Wang, W. X. Yuan, X. Wu, X. L. Chen, "Bulk GaN single crystals growth conditions by flux method", Journal of Crystal Growth, vol.247, no.3-4, pp. 275-278, 2003.

10. W. J. Wang, X. L. Chen, Y. T. Song, W. X. Yuan, Y. G. Cao, X. Wu, "Assessment of Li-Ga-N ternary system and GaN single crystal growth", Journal of Crystal Growth, vol.264, no.1-3, pp.13-16, 2004.

11. X. L. Chen, "Growth of bulk GaN single crystals by flux method", Sciences and Technology of Advanced Materials, vol. 6, no.7, pp. 766-771, 2005.

12. G. Wang, J. K. Jian, B. Song, X. L. Chen, W. J. Wang, Y.T. Song , "Bulk GaN single crystal: a reinvestigation of growth mechanism using Li$_3$N flux", APPLIED PHYSICS A-MATERIALS SCIENCE & PROCESSING, vol. 85, no.2, pp. 169-172, 2006.

13. M. Boc´kowski, I. Grzegory, B. Łucznik, T. Sochacki, M. Krys´ko, P. Strak, I. Dzie̜ cielewski, E. Litwin-Staszewska, and S. Porowski, "High nitrogen pressure solution growth of bulk GaN in ''feed-seed'' configuration", Phys. Status Solidi A, vol. 208, no.7, pp.1507-1510, 2011.

14. M. Kaminski, A. Waszkiewicz, S. Podsiadlo, J. Zachara, A. Ostrowski, W. Gebicki, A. Turos, and W. Strupinski, "GaN growth by sublimation sandwich method", phys. stat. sol. (c) , vol.2, no.3, pp.1065-1068, 2005.

15. D. Elwell, R. S. Feigelson , M. M. Simkins and W. A. Tiller, "Crystal growth of GaN by the reaction between gallium and ammonia", Journal of Crystal Growth, vol. 66, pp. 45-54, 1984.

16. C. M. Balkas and R. F. Davis, "Synthesis routes and characterization of high purity single – phase Gallium nitride", J. Am. Ceram. Soc., vol.79 , no.9, pp. 2309-2312, (1996.

17. S. T. Barry, S. A. Ruoff, and A. L. Ruoff, "Gallium nitride synthesis using lithium metal as nitrogen fixant", Chem. Mater., vol.10, pp. 2571-2574, 1998.

18. T. Hirano, A. Mabuchi, T. Sugiura, H. Minoura, "Synthesis of GaN crystal by the reaction of Ga with Li$_3$N in NH$_3$ atmosphere", Journal of crystal growth, vol.311, pp. 3040-3043, 2000.

19. C. H. Wallace, T. K. Reynolds, and R. B. Kaner, "Rapid synthesis of crystalline gallium nitride from solid precursors at atmospheric pressure", Chem. Mater., vol.11, pp. 2299-2301, 1999.

20. J. F. Janik and R. L. Wells, "Gallium Imide, {Ga(NH)3/2}n, a New Polymeric Precursor for Gallium Nitride Powders", Chem. Mater. , vol.8, pp.2708-2711, 1996.

21. Y. Kangawa, T. Wakigawa, and K. Kakimoto, "possibility of AlN solution growth using Al and Li$_3$N", Japanese Journal of Applied Physics, vol.6, No. 9A, pp.5785-5787, 2007.

22. T. Hirano, A. Mabuchi, T. Sugiura, H. Minoura, "Synthesis of GaN crystal by the reaction of Ga with Li$_3$N in NH$_3$ atmosphere", Journal of Crystal Gorwth, vol.311, pp.3040-3043, 2009.

23. J. Sangster and A. D. Pelton, "The Ga-Li (Gallium-Lithium) System", Journal of Phase Equilibria, vol. 12, no.1, pp. 33-36, 1991.

24. D. W. Osborne and H. E. Flotow, "Lithium nitride (Li$_3$N): heat capacity from 5 to 350K and thermochemical properties to 1086K", J. Chem. Thermodynamics. Vol. 10, pp.675-682, 1978.

25. S. Sinke, "Thermodynamic properties of the elements", Published November 1956 by American Chemical Society.
26. B. Raton, "CRC Handbook of Chemistry and Physics", 69TH Edition, 1988-1989, DAVID R. LIDE, Editor-in-Chief, CRC Press. Inc., Florida
27. B. Raton, "CRC Handbook of Chemistry and Physics", 90TH Edition, 2009-2010, DAVID R. LIDE, Editor-in-Chief, CRC Press. Inc. Florida
28. V. Y. Davydov, Y. E. Kitaev, I. N. Goncharuk, A. N. Smirnov, J. Graul, O. Semchinova, D. Uffmann, M. B. Smirnov, A. P. Mirgorodsky, R. A. Evarestov, "Phonon dispersion and Raman scattering in hexagonal GaN and AlN", PHYSICAL REVIEW B, Vol. 58, No.19, pp.12899-12907, 1998.
29. M. Kumar, M. Becker, T. Wernicke, R. Singh, "Multiphonon resonant Raman scattering non-polar GaN epilayers", *Appl. Phys. Lett.* Vol. 105, pp.142106, 2014.
30. Z. W. Si, Z. L. Liu, S. N. Zheng, X. M. Dong, X. D. Gao, J. F. Wang, K. Xu, "Yellow luminescence and carrier distribution due to polarity-dependent incorporation of carbon impurities in bulk GaN by Na flux", Journal of Luminescence, Vol.255, pp.119566,2023.

# Development of Innovative Drug Delivery System for Optimized Therapy of Traumatic Skin Conditions

Borislav Tzankov, Teodora Popova, Marta Slavkova, Christina Voycheva
Department of Pharmaceutical Technology, Medical University - Sofia, Bulgaria

## Abstract

The treatment of many traumatic skin conditions is often accompanied by the use of substances with bactericidal and bacteriostatic properties, most of which belong to the group of antibiotics. Unfortunately, the use of many classes of antibiotics such as sulfonamides, indicated in the treatment of skin injuries, is currently limited. This fact can be explained by various reasons, such as the pronounced tendency to slow down the wound healing process during their application. In this scientific paper, we propose the use of inorganic mesoporous silicate nanoparticles containing silver as a drug-delivering system for sulfadiazine. In our opinion, this approach would lead to overcoming the main limitations in the use of this representative of sulfonamides. In these first steps of the drug-delivery system development, we demonstrate the synthesis of silver-containing mesoporous silica nanoparticles and their successful loading with sulfadiazine. The structure of the obtained nanoparticles is proved, as they are distinguished by good physicochemical characteristics, which determine the high degree of load (37%) with a drug substance. The in-vitro release test shows delayed release of sulfadiazine within 14 hours.

**Keywords:** mesoporous silica, sulfadiazine, silver, wound healing;

## 1. Introduction

Sulfadiazine (SD) is a sulfonamide class which possess bacteriostatic activity against most gram-positive and gram-negative microorganisms. The mechanism of action of sulfonamides is based on inhibition of multiplication of bacteria by acting as competitive inhibitors of p-aminobenzoic acid in the folic acid metabolism cycle. However, nowadays there are some limitations in the use of sulfonamides. Due to the mechanism of action, bacterial sensitivity is similar for the various sulfonamides, so resistance to one sulfonamide indicates resistance to all the group. Moreover, soluble sulfonamide salts irritates the tissues due to its highly alkaline nature, so the parenteral administration is difficult. SD is widely used dermally in wound healing therapy as the bacterial resistance can be reduced by the use of combination of sulfadiazine and silver. In that combination, the silver ions binds with the DNA of the microorganism, releasing the sulfonamide which interferes with the intermediary metabolic pathway of the bacteria [1], [2], [3]. That combination is most effective against P. aeruginosa and the enterics, and equally effective as any antifungal drug against C. albicans and S. aureus. Usually silver-SD combination is used in the form of cream. However, there are also limitation in the dermal use of SD. Although it has some tissue-penetrating ability, it is limited to the surface epidermal layer [4]. Moreover, silver SD has been shown to retard wound healing, which is big limitation in its use [5]. In the recent years, there are some reports for the incorporation of SD and silver SD in different nanoparticles in order to avoid the limitations of the drug [6], [7]. Here we propose the preparation of an enhanced drug-delivery system based on mesoporous silica nanoparticles (MSN), containing a silver component as a carrier for the sulfonamide antibiotic sulfadiazine. The main advantage of the newly synthesized systems could be the potential for increased wound healing process.

## 2. Materials and methods

### 2.1. Materials

Sulfadiazine sodium (Merck, USA), tetraethylorthosilicate (Merck, USA), hexadecyltrimethylammonium bromide (Merck, USA), sulfadiazine sodium (Merck, Belgium), methanol (Merck, USA), N-N-dimethyl formamide, silver nitrate, deionized water.

### 2.2. Synthesis of nanosized mesoporous silica nanoparticles

Mesoporous silica nanoparticles were synthesized by a room temperature method as follows: tetraethylorthosilicate (TEOS: Merck, 800658) was used as a source of silicon. Hexadecyltrimethylammonium bromide (HDTMABr; BOH, 103912) was used as a surfactant template for preparation of the mesoporous material. Silver-containing MCM-41 were synthesized by reduction of silver nitrate with DMF using already described procedure (Preparation and characterization of Ag nanowires in mesoporous MCM-41 nanoparticles template by chemical reduction method). Firstly, 100 ml N-N-dimethyl formamide (DMF) was refluxed in a three-necked round-bottom flask at 70 °C for 1 h, then 2 g of MCM-41 and 20 ml DMF solution of 0.01 M silver nitrate were added to the solution at 60 °C. The reaction was continued at 60 °C for 24 h. After finishing the reaction, sample was filtered, washed several times with deionized water and dried under vacuum at room temperature.

### 2.3. Sulfadiazine loading

100 mg of SD sodium were dissolved in 10 ml of deionized water under permanent stirring at 37˚C. 100 mg of MSN or MSN/Ag were added to the mixture and the system was incubated at 37˚C until the full water evaporation. Dried samples were further triple washed with methanol and dried at room temperature. The samples were named MSN_SD and MSNAg_SD.

### 3. Characterization

Particle size, polydispersity index and zeta potential of loaded and unloaded nanoparticles were determined using a Zetasizer Nano ZS (Malvern Instruments, UK). The samples were dispersed in deionized water and measured at a scattering angle of 90° and 25°. Determination of nanoparticle morphology was carried out by transmission electron microscopy (JEOL JEM 2100 HR STEM - 200KV; point-resolution 0.23nm). Electronic absorption spectra of Ag was represent by UV-Vis spectroscopy. Attenuated total reflection infrared (ATR-FTIR) spectra over the spectral region from 400 to 4000 cm−1 were recorded by spectrometer Nicolette 400 (Thermo Fisher Scientific, USA).

The SD content of nanoparticles was estimated in deionized water using the extraction method. The desired amount of SD-loaded dry nanoparticles was extracted in 100 mL of deionized water at room temperature under stirring. After that, 3 ml samples were centrifuged (15 000 rpm, 15 min (High-Speed Mini Centrifuge Dragon Lab D2012 plus)) and the SD content in the supernatant was measured with a UV spectrophotometer (Thermo Scientific Evolution 300, Madison, WI, USA) at a wavelength of 270 nm. The percent of entrapment efficiency was calculated according to the following equation.

The in vitro drug release from the nanoparticles was performed as follows: 5 mg pure SD, as well as MSNAg_SD (equivalent to 5 mg SD), were placed into 50 ml buffer (pH 5.5). The incubator shaker (Julabo Shake Temp SW23, Germany) was kept at 35°C under permanent stirring (100 rpm). Samples (2 ml) were withdrawn at appropriate time intervals, as particles were removed from solution by centrifugation at 15,000 rpm for 10 min (High-Speed Mini Centrifuge Dragon Lab D2012 plus) and the concentration of the released SD was determined by UV–vis spectrophotometry.

### 4. Results and discussion

DLS measurement analysis show particle size in the nano range for obtained samples (Table 1). The nanoparticle diameter increased insignificant with the addition of Ag-compound in the preparation scheme and further loading of the drug. Zeta-potential measurements show negative values, typical for the mesoporous silica materials. However, significant change is observed after the SD incorporation as the zeta-potential approaches neutral values, which inevitably leads to a decrease in physical stability. This fact could describe the change of the polydispersity index after drug-loading procedure.

**Table 1.** Phisico-chemical properties of empty and drug-loaded particles

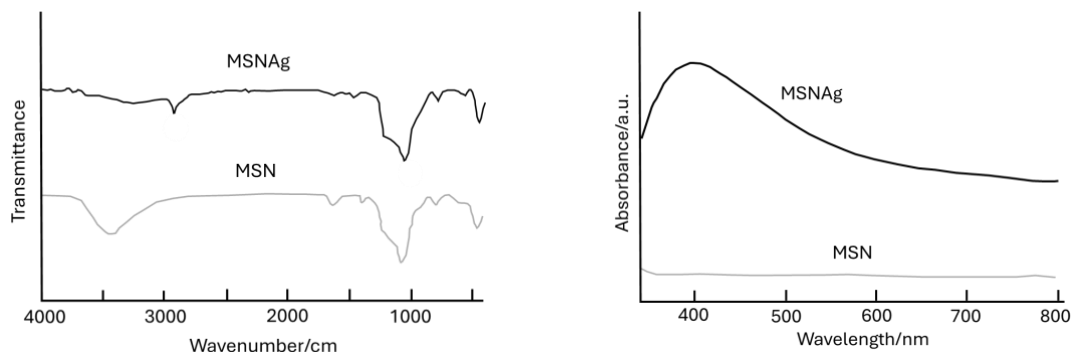|  | Size (nm) | Zeta-potential (mV) | Polydispersity index | Drug loading (%) |
|---|---|---|---|---|
| MSN | 371.3 | -21.2±6 | 0.43 | - |
| MSNAg | 396.6 | -29.5±4 | 0.37 | - |
| MSNAg_SD | 405.7 | -5.9±3 | 0.77 | 37 |



**Figure 1.** FTIR (left) and UV-Vis (right) spectra of parent MSN and silver-containing MSNAg samples

FT-IR spectras of the samples are shown in Fig. 1. The samples have three strong peaks at around $456\,cm^{-1}$, $804\,cm^{-1}$ and $1075\,cm^{-1}$, which are assigned to the symmetric stretching vibration modes of Si-O-Si framework. The bands at 1633 and $3424\,cm^{-1}$ are ascribed to the bending vibration and stretching modes of single bond OH group, respectively [8]. The absorption peak at $955\,cm^{-1}$ in MSN sample can be assigned to the characteristic mode of silanol groups. This absorption peak almost disappeared in MSNAg suggesting the silanol groups were replaced by other groups during modification process. In addition, the characteristic peaks at $2925\,cm^{-1}$ demonstrated the existence of single bond $NH_2$ functional groups in MSNAg sample [9].

UV-Vis method was use to represents the electronic absorption spectra of MSNAg in liquid. The results supports already published data [10]. The measurements present a broad absorption band at 415 nm, which can be associated with oscillation of conduction band electrons of Ag known as the surface plasmon resonance [11].

TEM images of MSN and MSNAg (Figure 2) show the samples consisted of many worm-like domains which is character for mesoporous silica particles. The channels are with relatively uniform sizes and homogenous dispersed. The particles are spherical, with relatively uniform size. The addition of Ag-compound in the structure led to some changes in the particle` channels.
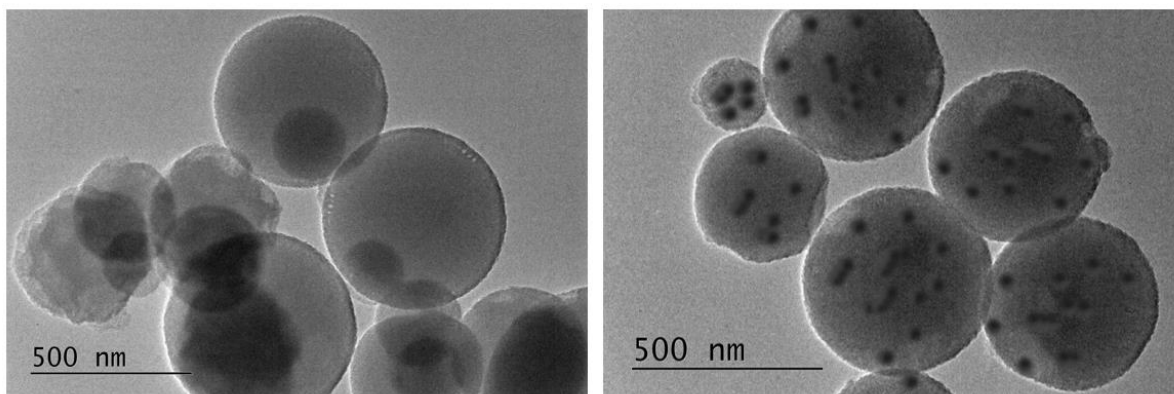


**Figure 2.** TEM of parent MSN (left) and silver-containing MSN (right)

The in-vitro comparison study of the solubility of SD and its release from MSNAg show relatively fast solubility of the drug in the used conditions (almost 100% for 2h). The incorporation of the drug into MSNAg led to low initial burst release and sustained release in 14 hours.
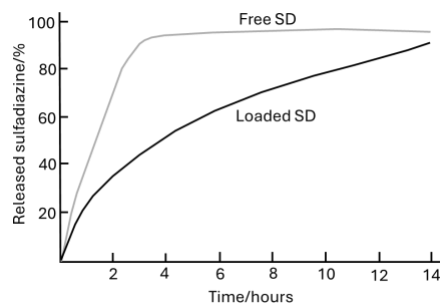


**Figure 3.** In-vitro comparison between the solubility of free SD and drug release from MSNAg_SD

FT-IR The samples have three strong peaks at around 456 cm−1, 804 cm−1 and 1075 cm−1, which are assigned to the symmetric stretching vibration modes of Si-O-Si framework. The absorption peak at 955 cm−1 in MSN sample can be assigned to the characteristic mode of silanol groups. This absorption peak almost disappeared in MSNAg suggesting the silanol groups were replaced by other groups during modification process. In addition, the characteristic peaks at 2925 cm−1 demonstrated the existence of single-bond NH2 functional groups in MSNAg sample.

UV-Vis method was use to represents the electronic absorption spectra of MSNAg in liquid. The results supports already published data. The measurements present a broad absorption band at 415 nm, which can be associated with oscillation of conduction band electrons of Ag known as the surface plasmon resonance

We assumed these observations proved the incorporation of Ag-compound in the MSN structure.

## 5.  Conclusion

An innovative drug delivery system for optimized therapy of traumatic skin conditions based on mesoporous silicate nanoparticles containing silver and loaded with sulfadiazine, has been successfully developed. Through a set of physicochemical methods, the structure of the particles and the high degree of drug loading have been proven. The release test showed delayed release for an extended period of time. The preliminary tests carried out show that the developed nanosystems have a high potential for the inclusion of substances with bactericidal and bacteriostatic effects in order to accelerate wound healing in skin injuries.

**Acknowledgements**

**References:**

1. J. Heggers, 'The Use of Antimicrobial Agents', *Clinics in Plastic Surgery*, vol. 6, no. 4, pp. 545–551, Oct. 1979, doi: 10.1016/S0094-1298(20)32017-4.
2. J. P. Heggers, M. C. Robson, and L. G. Phillips, *Quantitative Bacteriology: Its Role in the Armamentarium of the Surgeon*. CRC Press, 1990.
3. J. A. Moncrief, 'Topical antibacterial treatment of the burn wound', *Burns: a team approach. Philadelphia: WB Saunders*, pp. 250–269, 1979.
4. A. J. Gear *et al.*, 'A new silver sulfadiazine water soluble gel', *Burns*, vol. 23, no. 5, pp. 387–391, 1997.
5. M. J. Muller, M. A. Hollyoak, Z. Moaveni, T. L. H. Brown, D. N. Herndon, and J. P. Heggers, 'Retardation of wound healing by silver sulfadiazine is reversed by Aloe vera and nystatin', *Burns*, vol. 29, no. 8, pp. 834–836, 2003.

6.  A. Santagata *et al.*, 'Production of silver-silica core-shell nanocomposites using ultra-short pulsed laser ablation in nanoporous aqueous silica colloidal solutions', *Journal of Physics D: Applied Physics*, vol. 48, no. 20, p. 205304, 2015.

7.  G. Sandri *et al.*, 'Wound dressings based on silver sulfadiazine solid lipid nanoparticles for tissue repairing', *European Journal of Pharmaceutics and Biopharmaceutics*, vol. 84, no. 1, pp. 84–90, 2013.

8.  Z. Zhang *et al.*, 'Pt nanoparticles supported on amino-functionalized SBA-15 for enhanced aqueous bromate catalytic reduction', *Catalysis Communications*, vol. 105, pp. 11–15, 2018.

9.  E. Vyskočilová, I. Luštická, I. Paterová, L. Machová, and L. Červenỳ, 'Modified MCM-41 as a drug delivery system for acetylsalicylic acid', *Solid state sciences*, vol. 38, pp. 85–89, 2014.

10. X. Zhang, Q. Xu, and I. Saiki, 'Quercetin inhibits the invasion and mobility of murine melanoma B16-BL6 cells through inducing apoptosis via decreasing Bcl-2 expression', *Clin Exp Metastasis*, vol. 18, no. 5, pp. 415–421, Sep. 2000, doi: 10.1023/A:1010960615370.

11. C. A. Foss Jr, 'Gabor L. Hornyak, Jon A. Stockert, and Charles R. Martin', *J. Phys. Chem. B*, vol. 98, pp. 2963–2971, 1994.

# Preparation, chemical–physical characterization of composite hydro-gels – nanoparticles of Ag and Ag$_2$MoO$_4$. Stability analysis and biomedical applications

Sara Calistri[1,2], Alberto Ubaldini[2], Antonietta Rizzo[2], Alessandra Strafella[3], Chiara Ciantelli[4], Carmela Maria Cellamare[2]

[1] Department of Pharmacy and Biotechnology, Alma Mater Studiorum, University of Bologna, Bologna, 40126, Italy, sara.calistri2@unibo.it

[2] ENEA, Via Martiri di Monte Sole 4, 40129 Bologna (Bo), Italy, alberto.ubaldini@enea.it; antonietta.rizzo@enea.it; carmela.cellamare@enea.it

[3] ENEA, Via Ravegnana, 186, 48018 Faenza (Ra), alessandra.strafella@enea.it

[4] ENEA, C.R. Brasimone, 40032, Camugnano (BO), chiara.ciantelli@enea.it

**Abstract**

Bacterial infections and antibiotic resistance are critical global health concerns. This study is aimed to the synthesis and characterization of hydrogels incorporating Ag and Ag$_2$MoO$_4$ nano- and microcrystals, known for their antibacterial properties. These composite materials promise to combine the useful properties of both parent systems, limiting all possible adverse effects of nanoparticles.

Hydrogels charged with nanocrystals are an emerging and promising platform for biomedical applications, offering enhanced antimicrobial efficacy and targeted drug delivery capabilities to combat infectious diseases and antibiotic resistance.

Highly biocompatible hydrogels such as alginates and silver-based nanoparticles, which are very versatile and functionalized, have been chosen.

**Keywords:** Hydrogel, nanoparticles, chemical-physical characterization, antimicrobial tests.

## 1. Introduction

Gels are composite materials consisting of a three-dimensional (3D) polymer network embedded within a liquid phase, which is incorporated into a solid structure [1]. The polymeric network incorporates the liquid and, in turn, the liquid prevents the network from collapsing, because of its surface tension. When the liquid phase is water, they are called hydrogels. Hydrogels and other gels possess exceptional physicochemical properties that are typically adjustable and tunable to meet the specific requirements of their diverse applications.

They are used for many technological advanced functions such as lens or actuators and above all they have been extensively applied in the biomedical field ranging for tissue regeneration and disease therapies. They are used as intraocular vitreous filler, for tissue engineering (reparation and healing of skin, cartilage, cardiovascular tissues…) [1, 2], for wound dressing, for controlled drug delivery systems, and many others. Additionally, modern synthesis techniques now allow the synthesis of hydrogels with biocompatible polymer matrices, such as alginates and chitosan. This biocompatibility significantly enhances their suitability for biomedical applications [2].

These already excellent properties can be further increased when nanoparticles of useful inorganic materials are added to the hydrogels. Metal and oxide nanoparticles are known for their excellent bactericidal, anti-mycobial and generally antimicrobial properties. They can be used as carriers of drugs and other therapeutic agents.

Therefore, hydrogel-nanoparticle composites can effectively integrate the beneficial properties of both parent systems while minimizing any potential adverse effects of nanosystems. Nanocrystal-loaded hydrogels are a promising platform for biomedical applications, largely due to the vast array of materials that can be synthesized as nanoparticles. These nanoparticles often possess unique and highly specific capabilities, making them exceptionally versatile for diverse medical uses. [3]

This work is focused on the synthesis and characterization of chemically stabilized alginate hydrogel incorporating Ag and Ag$_2$MoO$_4$ nano and microcrystals, well known for their antibacterial properties. An

effective synthesis method has been performed for the preparation of the polymer matrix and for the incorporation of the particles.

The final composite samples have been characterized by Scanning Electron Microscopy (SEM) for morphology, by Raman spectroscopy for chemical composition, by X-Ray Diffraction (XRD) for crystalline structure and by Differential Scanning Calorimetry (DSC) – Thermo Gravimetry (TC) for thermal behaviour.

## 2. Experimental

### 2.1. Materials and methods

The synthesis of the hydrogel has been performed dissolving 2 g of sodium alginate in 100 mL of water at 60°C, adding 15 g of acrylamide, 0.01 g/10 mL of N,N'-methylenebisacrylamide (MBAA), and a potassium persulfate initiator. Subsequently, 0.2 mL of N,N,N',N'-tetramethylethylenediamine (TEMED) has been added [4].

Silver nanoparticles have been prepared submerging the hydrogel in a 20 mL solution of $AgNO_3$ (10 mM) for 24 hours in order to a complete diffusion inside the gel structure, followed by immersion in a 5 mM $NaBH_4$ solution for an additional 24 hours at room temperature.

$Ag_2MoO_4$ microcrystals have been prepared in a similar way by immerging the hydrogel in a 20 mL solution of $Na_2MoO_4$ (5 mM) for 24 hours, followed by immersion in a 5 mM $AgNO_3$ solution for an additional 24 hours at room temperature.

### 2.2. Characterization

Raman spectra of the compounds and mixtures were acquired, at room temperature, by a BWTEK i-Raman plus spectrometer equipped with a 785 nm laser in the range of $100 - 3500$ cm$^{-1}$ with a spectral resolution of 2 cm$^{-1}$. The morphological characterization of the samples has been performed by Scanning Electron Microscopy (SEM FEI QUANTA INSPECT S). Thermal analysis was performed for each sample using an STA 409C simultaneous analyzer (Netzsch, Selb, Germany) equipped with DSC/TG sample carrier system, supporting an S type thermocouple. During the thermal program set up in the tests, the change in sample mass (TG expressed as % mass loss) and in heat flow due to transformation from one state to another or other physical phenomena (DSC expressed as mW/mg) were measured. DSC/TG analyses were performed under dynamic air atmosphere with a flow rate of 100 ml/min and a heating rate of 5 °C/min up to 650°C. To perform these analyses approximately 13mg of samples were weighed and placed in an 85-μl volume $Al_2O_3$ sample crucible. Microbiological analysis has been conducted according to ISO 9308-1:2014 Water quality — Enumeration of Escherichia coli and coliform bacteria.

## 3. Results and discussion

Alginate-based hydrogels are commonly formed by replacing sodium ions with divalent cations like $Ca^{2+}$, $Sr^{2+}$, or $Zn^{2+}$, resulting in physical cross-linking zones. However, these gels often lack long-term stability and homogeneity. To address this, chemical cross-linking via acrylamide polymerization is preferred, as it creates a robust three-dimensional network that effectively supports the alginate chains. Figure 1 shows a schematic depiction of the hydrogel formation.
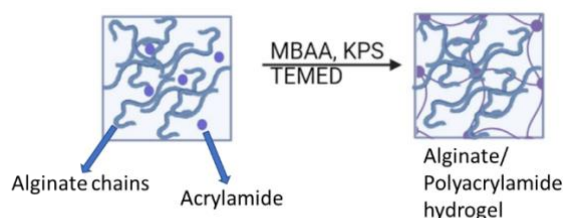


**Fig. 1**: Hydrogel formation

The gels thus prepared show excellent mechanical properties such as elasticity, toughness and resistance, a great ability to reversibly absorb large quantities of water, as demonstrated by swelling studies [5]. In particular, they can undergo numerous absorption/distraction cycles without losing their chemical-physical characteristics and this makes them particularly attractive for biomedical applications.

These hydrogels also show great thermal stability, as can be observed in Figure 2, which shows the DSC - Tg curves of the pure dry hydrogel. It is worth noting that the gel is very stable up to about 150 °C and that between room temperature and 150 °C there is only a small loss of mass associated with the evaporation of residual water. The last step is the most exothermic and indicates the complete degradation of the matrix occurs no earlier than 400 °C with the peak at approximately 520 °C and it is complete at about 580 °C. Between 200 and 400 °C some exothermic degradation reactions occur which are associated with mass losses (the polymer composed of multiple types of monomers).
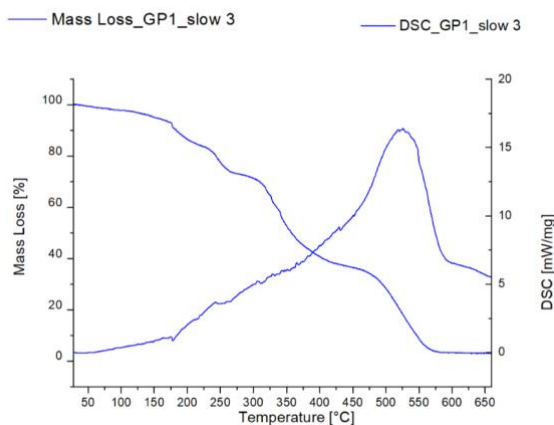


**Fig. 2**: Thermogravimetry-differential scanning calorimetry curve of pure hydrogel

The hydrogels' ability to absorb water facilitates the in situ formation of nanoparticles and microcrystals, allowing them to be generated directly within the polymer matrix. Gel samples were allowed to adsorb solutions of $AgNO_3$ or $Na_2MoO_4$ which diffused completely into the matrix. Subsequently, diluted solutions of $NaBH_4$ and $AgNO_3$ were diffused into the samples, which induced the following reactions:

1. $AgNO_3 + NaBH_4 \rightarrow Ag + NaNO_3 + \frac{1}{2} B_2H_6 + \frac{1}{2} H_2$
2. $Na_2MoO_4 + AgNO_3 \rightarrow Ag_2MoO_4 + 2 NaNO_3$

This method enabled the controlled growth of silver and submicrometer silver molybdate particles, known for their strong antimicrobial properties, directly within the hydrogel matrix. Figure 3A shows a SEM image of hydrogel charged by $Ag_2MoO_4$ crystals and Figure 3 shows its Raman spectrum [6].
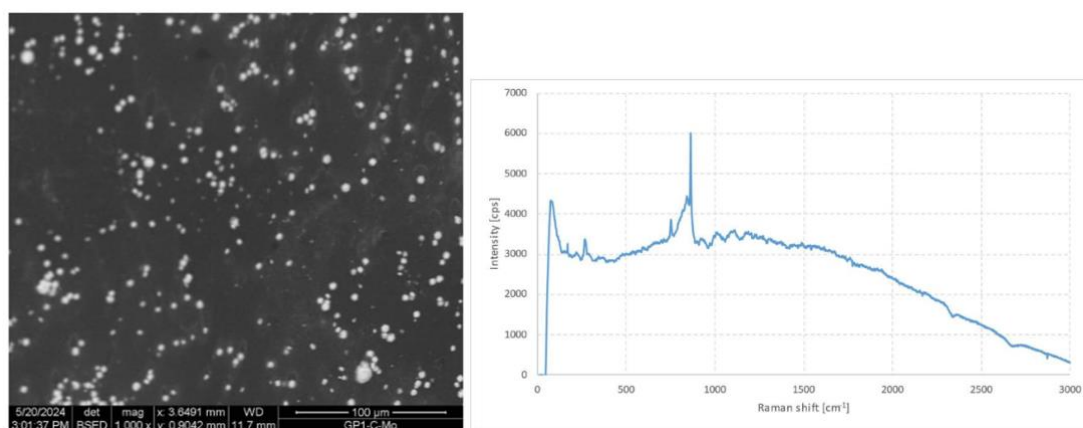


**Fig. 3**: SEM image of $Ag_2MoO_4$ charged hydrogel (BSE detector, mag 1000x) (A) and Raman spectrum of the same sample (B)

It is interesting to note that the crystals have a very homogeneous distribution and constant size; their morphology is different from that obtained by free precipitation from aqueous solutions (typically octahedral [6]), indicating that their growth is determined by specific diffusion processes in the polymeric matrix. The spectrum is characterized by the typical functional groups of these polymers and by intense bands, due to the normal modes of $Ag_2MoO_4$, which are dominated by the vibrations of the $MoO_4$ tetrahedra.

Composite hydrogels have proven to be very effective in controlling the growth of *Escherichia Coli* bacterial colonies [7]. In the reference samples, i.e. those without gels, the growth of numerous colonies occurs (while in the blacks, treated only with sterile water, this does not occur meaning that any possible growth is not due

to external contamination). The gels were placed on the surface of the filters where bacteria were present. In the case of pure gels, colonies grew in a number comparable to the reference samples, indicating that the matrix is quite biocompatible, while gels loaded showed excellent antibiotic properties, completely inhibiting the growth of cell colonies. and this cannot be due to external factors, such as, for example, lack of oxygen or nutrients. At the same time, these composite gels were stable and did not degrade, suggesting that the dispersion of the nanoparticles is limited. Figure 4 shows the antimicrobial tests performed using pure hydrogel and Ag-charged one.
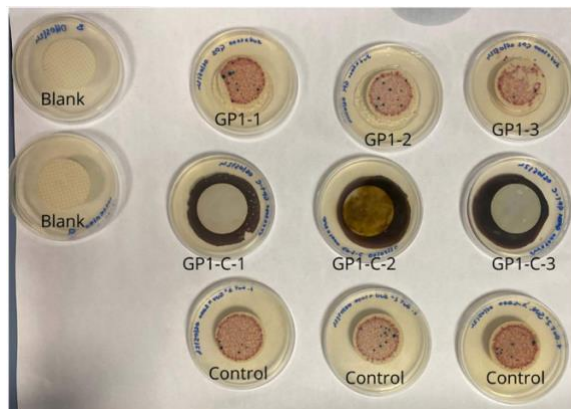


**Fig. 4**: Antimicrobial tests performed using a pure hydrogel and Ag- charged hydrogel

For pure gels, no statistically significant differences were noted in the number of bacterial colonies grown after 24 hours of incubation compared to the control, charged gels completely inhibited growth, proving to be very effective.

## 4. Conclusion

Preliminary synthesis and characterization experiments of biocompatible hydrogels loaded with nano/micro crystals of different nature have been carried out.

The synthetized hydrogels have been proven to be chemically stable and uniform. The particles were found to be uniformly dispersed in the matrix and the functionalized hydrogels exhibited excellent antimicrobial properties.

## References

1. Enas, M. A.; "Hydrogel: Preparation, characterization, and applications: A review", Journal of Advanced Research, 6, 2015, 105-121, https://doi.org/10.1016/j.jare.2013.07.006.
2. Sánchez-Cid, P.; Jiménez-Rosado, M.; Romero, A.; Pérez-Puyana, V.; "Novel Trends in Hydrogel Development for Biomedical Applications: A Review". Polymers 2022 26;14(15):3023. doi: 10.3390/polym14153023
3. Jiang, Y.; Krishnan, N.; Heo, J.; Fang, RH.; Zhang, L.; "Nanoparticle-hydrogel superstructures for biomedical applications". J Control Release. 2020, 10;324:505-521. doi: 10.1016/
4. Lei, X.; Wu, Y.; Peng, X.; Zhao, Y.; Zhou, X.; Yu, X. Research on alginate-polyacrylamide enhanced amnion hydrogel, a potential vascular substitute material. Mater. Sci. Eng. C 2020, 115, 111145. https://doi.org/10.1016/j.msec.2020.111145
5. Feng, W.; Wang, Z.; "Tailoring the Swelling-Shrinkable Behavior of Hydrogels for Biomedical Applications", Adv. Sci. 2023, 10, 2303326
6. Calistri, S.; Gessi, A.; Marghella, G.; Bruni, S.; Ubaldini, A. Characterization and Formation Mechanism of $Ag_2MoO_4$ Crystals via Precipitation Method: Influence of Experimental Parameters and Crystal Morphology. Crystals 2024, 14, 254. https://doi.org/10.3390/cryst14030254.
7. Varaprasad, K., Mohan, Y.M., Ravindra, S., Reddy, N.N., Vimala, K., Monika, K., Sreedhar, B. and Raju, K.M. (2010), Hydrogel–silver nanoparticle composites: A new generation of antimicrobials†". J. Appl. Polym. Sci., 115: 1199-1207. https://doi.org/10.1002/app.31249

# Improvement of Photosensor Properties of ZnO Films by Using the Features of Nanostructured State

S. Dukarov[1], S. Petrushenko[*1,2], K. Adach[2], M. Fijalkowski[*2], A.Fedonenko[2], V. Sukhov[1]

[1] V. N. Karazin Kharkiv National University, 4 Svobody Sq., Kharkiv, 61022
[2]Technical University of Liberec
Studentská 1402/2
461 17 Liberec 1, Czech Republic, Serhii.Petrushenko@tul.cz, Mateusz.Fijalkowski@tul.cz

**Abstract**

The work is devoted the UV-photosensitivity of ZnO films, which are obtained by chemical methods. Two geometries of resistive photodetector were considered. In horizontal type detectors, the eclectic current propagates parallel to the substrate. In this case, the distance between the electrodes is about 2 cm. In detectors of vertical type, the electric current propagates in perpendicular direction. In this case there is only a micron-thick photosensitive layer between the electrodes. In addition to the detector geometry, the influence of the microstructure of the ZnO film on its photosensitivity was also investigated. It is shown that the photosensitivity varies strongly depending on the detector geometry and microstructure of the films. Physical considerations connecting the nanocomposite state of the films with their improved sensory properties are proposed. It is shown that there is a presence of two mechanisms of photosensitivity connected with the presence of two types of surface in the studied samples. Physical considerations on the nature of photosensitivity and options for improving the rate performance of ZnO layers based on changes in their morphology are proposed. It has been showed that vertical type detectors, in which the photosensitive layer is solid nanocrystalline, have the best photosensitivity.

**Keywords:** photodetectors, UV radiation, ZnO, nanocomposites, thin films

## 1. Introduction

Measuring UV radiation, especially its A component (320-400 nm), is an important task of modern technologies. Zinc oxide layers are a promising material of detectors meeting these conditions. Such films can be obtained on a variety of substrates, including fabric ones, using simple and scalable chemical methods. Such layers are non-toxic, and their cost is favorable for implementation. Unfortunately, despite the potential prospects, the photosensitivity, and reaction rate of ZnO-based detectors appear/occur to be inferior to industrial samples based on Si, SiC, and GaN. This makes it important to search for ways to increase the photosensitivity and response rate of ZnO-based detectors. One of the ways to realize this task is the use of the size factor. However, before this, it is necessary to clarify the physical features of nanostructured photodetectors. This work is devoted to the establishment of the physical essence of the relationship between the photosensory properties of ZnO films, the main mechanism of photosensitivity and the microstructure of the sample.

## 2. Experimental

Two methods of deposition of functionalized films were used in this work. The layer-by-layer chemical adsorption method (SILAR) is described in [1]. This semiconductor layers deposition method involves the sequential conducting of a series of cycles. Each cycle involves immersing the substrate into a cationic precursor, namely an aqueous 1 M $ZnSO_4$ solution, an anionic precursor, as which distilled water was used at 80-90 °C, and washing in room temperature water. A chemical reactor with microwave heating (ERTEC Magnum II, Poland) was used for the hydrothermal method. In this method the ZnO layer was deposited using a solution of zinc nitrate hexahydrate and hexamethylenetetramine in absolute ethanol. Aqueous solutions of zinc nitrate hexahydrate and hexamethylenetetramine (HMTA) were prepared by mixing zinc nitrate hexahydrate and hexamethylenetetramine to obtain 50 ml solution. Two series of samples were obtained. In the first series, the molar concentrations of zinc nitrate hexahydrate and hexamethylenetetramine were 100 mM and 100 mM. These samples are hereinafter labelled as 100_100. In the second series of films deposited by the hydrothermal method,

the molar concentrations of zinc nitrate hexahydrate and hexamethylenetetramine were 100 mM and 50 mM. The samples in this series are labelled as 100_50. After preparation of the solution, the substrate with the seeding layer was immersed in the solution and placed in a UHF reactor. The reaction temperature was reached about 300 s after switching on the microwave radiation and was maintained above the reaction value for 1400 s. At the same time, microwave radiation with a power of 360 W took place during the first 300 s of the reaction. The pressure in the reactor was maintained at 15-18 bar. Films for horizontal-type detectors (Fig. 1a) were deposited on glass substrates with an active area of 1×2 cm. To record electrical resistance, clamping electrical contacts based on 0.5×2 cm aluminium strips were used (Fig. 1a). To create horizontal detectors (Fig. 1b), films deposited on carbon fabric were used. In this case, the carbon fabric acted as one of the electrodes. A glass plate with an ITO layer deposited on one of its sides was used as a transparent electrode.
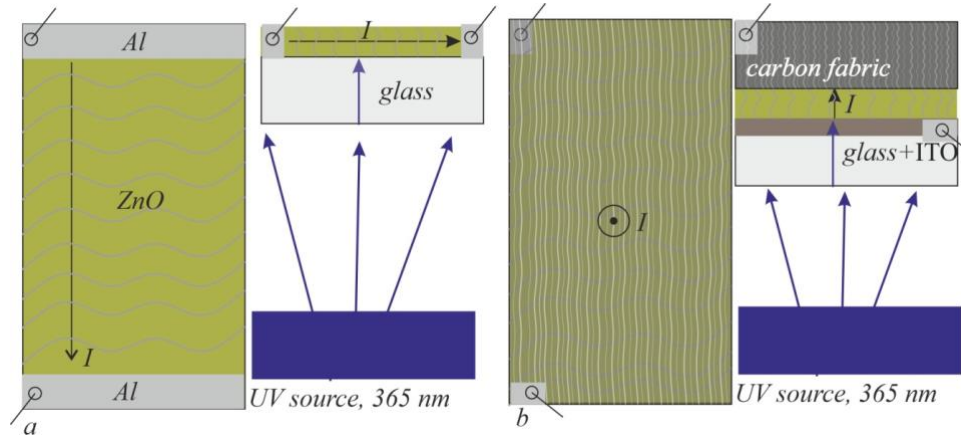


**Fig. 1**: Scheme of detectors of horizontal (a) and vertical (b) types.

## 3. Results and discussion

Several types of ZnO films of diferernts microstructures were obtained (Fig.2). The films deposited by the SILAR method are solid and nanocrystalline. The most probable size of crystallites in such samples is 10–12 nm. It changes slightly when passing from glass substrate to carbon substrate. Films deposited by the hydrothermal method consist of monocrystalline hexagons. Their most probable size is 40–50 nm.
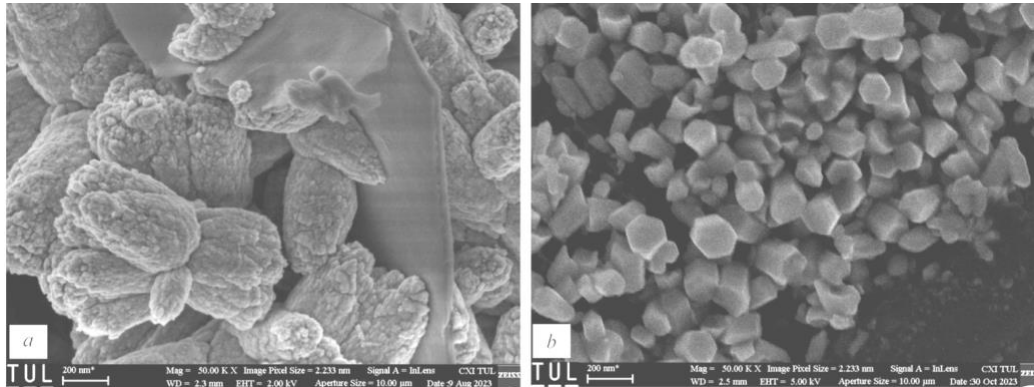


**Fig. 2**: SEM images of films deposited by SILAR (a) and hydrothermal methods (b).

Fig. 3a shows an example of photovoltaic curves obtained for horizontal and vertical type detectors formed on the basis of ZnO films deposited by the SILAR method on glass and fabric substrates. In order to preserve the nanostructure, unlike, for example, [2, 3], the samples were not subjected to annealing. It can be seen that horizontal detectors have a noticeable photosensitivity: the current through the sample increases by 10% during UV radiation. Significantly higher photosensitivity is observed in detectors of vertical type (Fig. 3a). In such samples, the electric current under UV radiation increases more than three times. That is, the photosensitivity of

such samples exceeds 300%. At the same time, the active area of the vertical detector is twice smaller than the area of the horizontal detector. Compared to the sensitivity of the samples deposited by the SILAR method, the sensitivity in the layers deposited by the hydrothermal method is slight (Fig. 3b). Even in the configuration of the vertical detector, it is only 5% in the 100_100 series samples and 2% in the 100_50 series films.
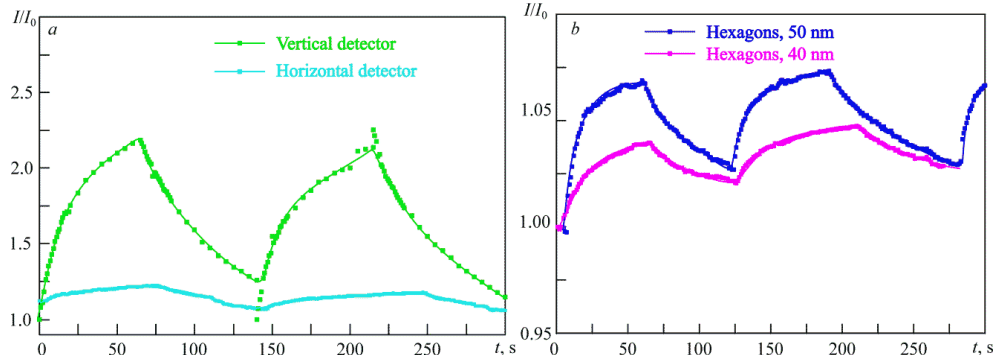


**Fig. 3**: Time dependence of the specific photocurrent for SILAR-deposited horizontal and vertical type detectors (a). The typical value of electrical resistance in horizontal detectors constitutes a few megohms and is measured in tens of kilohms in vertical detectors. The dependence on time of photocurrent in vertical type detectors based on ZnO films deposited by hydrothermal method (b).

A convenient way for approximating the dependence of the specific photocurrent on time for ZnO films is the biexponential function [4]:

$$I = I_0 + A_1 e^{\frac{t}{t_1}} + A_2 e^{\frac{t}{t_2}} \tag{1}$$

Here $I = I_{UV}/I_{dark}$, where $I_{UV}$ and $I_{dark}$ are the value of photo and dark current, respectively. $t$ — exposure time. Thus, the photocurrent rise rate is described by the time parameters $t_1$ and $t_2$. The biexponential form of equation (1) indicates the existence of two mechanisms, the superposition of which provides photosensitivity. As a rule, the photosensitivity of zinc oxide is connected with the processes of adsorption and desorption of oxygen [5] occurring on the surface of the substance. An important role in these phenomena is played by the formation of electron-hole pairs that contribute to the desorption of previously adsorbed oxygen [5]. However, this expression turned out to be poorly applicable to horizontal-type detectors. For such samples, the value of $t_2$ determined at approximation of experimental dependences by expression (1), is counted in millions of seconds. This indicates that only one mechanism of photosensitivity prevails in horizontal detectors at the used voltage of shifting. At the same time, expression (1) is well suited to describe the detectors of the vertical type. The obtained, with this, values of characteristic time are counted in tens of seconds and look typical for unmodified zinc oxide films. For example, for vertical detectors obtained by the SILAR method, the time constants (1) are 5.5 s and 25 s. For detectors obtained by the hydrothermal method, the time constants are 5.5 s and 28 s in 100_100 series films and increase to 8 s and 60 s in 100_50. However, in such films, the use of equation (1) is often less reliable. In separate cases, when approximating the experimental dependencies by this equation, the time constants and multipliers $A_1$ and $A_2$ become equal. In other cases, one of the time constants is again measured in billions of seconds. Thus, and these detectors look as restrictedly described by equation (1). Since the photosensitivity curves obtained for horizontal detectors are poorly described by functions of the form (1) when $A_1 \neq A_2 \neq 0$, it was considered to approximate these data that $A_2 = 0$, i.e., expressions of the form (1) were used:

$$I = I_0 + A_1 e^{-\frac{t}{t_1}} \tag{2}$$

The time constant determined in this way for horizontal detectors is about 30 s. If we describe the behavior of vertical detectors by a function of the form (2), then t1 for films deposited using SILAR is 20-23 s. A similar value, namely 22 s is also observed in the 100_50 films. A slightly lower value of time constant takes place in 100_100 films. In these films, the time constant is 12 s. To quantitatively describe the relaxation processes of

photodetectors, the dark regions of photovoltaic curves were also approximated by exponential functions of the form (1) and (2). It was found that the use of the biexponential function (1) is not a reliable way to describe the relaxation of the photodetector. In most cases, it is the functions with a single term that proved to be the most reliable way of approximating such functions. As for the specific values of the time constants, they are 47 s for the 100_100 series and 36 s for 100_50. For vertical detectors based on layers deposited using SILAR, the constant time of photocurrent relaxation is 35 s. For detectors of horizontal type, the time constants increase up to 80 s. Comparing the data obtained for different detector configurations, we can conclude that the two mechanisms of photosensitivity characteristic of ZnO are best manifested in vertical detectors deposited by the SILAR method. The two-stage nature of photosensitivity is less obviously manifested in layers deposited by the hydrothermal method. In detectors of horizontal type, one mechanism of photosensitivity prevails.

## 4. Conclusion

Semiconductor detectors of UV radiation that can operate at a low voltage of shifting and can be easily integrated into fabric substrates have been proposed. It is shown that the films obtained using a simple and cheap method of synthesis in aqueous SILAR solutions provide better sensitivity than the layers, for the deposition of which a more complex method of hydrothermal synthesis with UHF heating was used. It is shown that there is a presence of two mechanisms of photosensitivity connected with the presence of two types of surface in the studied samples. Physical considerations on the nature of photosensitivity and options for improving the rate performance of ZnO layers based on changes in their morphology are proposed.

## Acknowledgements

## References

1.  Klochko, N., Klepikova, K., Khrypunova, I., Kopach, V., Petrushenko, S., Zhadan, D., ... & Khrypunova, A. "Texible in-plane thermoelectric modules based on nanostructured layers ZnO and ZnO:In," *Materials Today: Proceedings*, vol. 62, pp. 5729–5738, 2022. https://doi.org/10.1016/j.matpr.2022.02.341
2.  Barnett, C. J., Smith, N. A., Jones, D. R., Maffeis, T. G., & Cobley, R. J.  "Effects of vacuum annealing on the conduction characteristics of ZnO nanosheets, " *Nanoscale research letters*, vol. 10, p. 368, 2015. https://doi.org/10.1186/s11671-015-1066-1
3.  Ghosh, R., Paul, G. K., & Basak, D. "Effect of thermal annealing treatment on structural, electrical and optical properties of transparent sol–gel ZnO thin films," *Materials research bulletin*, vol. *40,* no 11, pp. 1905–1914, 2005. https://doi.org/10.1016/j.materresbull.2005.06.010
4.  Jiang, H., Li, L., Feng, S., & Lu, W. "Nanodiamond enhanced ZnO nanowire based UV photodetector with a high photoresponse performance,". *Physica E: Low-dimensional Systems and Nanostructures*, vol. 104, pp. 314–319, 2018. https://doi.org/10.1016/j.physe.2018.07.041
5.  Yuan, B., Zheng, X. J., Chen, Y. Q., Yang, B., & Zhang, T. "High photosensitivity and low dark current of photoconductive semiconductor switch based on ZnO single nanobelt,". *Solid-State Electronics*, vol. 55, no 1, pp. 49–53, 2011. https://doi.org/10.1016/j.sse.2010.09.002

# Non-carboxylated and Carboxylated Mesoporous Carbon Nanoparticles Loaded with Bicalutamide – an Advanced Nanosystem for Combined Chemo-photothermal Therapy

T. Popova[1], B. Tzankov[1] , M. Slavkova[1], Y. Yordanov[1], V. Georgieva[1], D. Stefavova[1], V. Tzankova[1], D. Tzankova[1], Iv. Spasova[2], D. Kovacheva[2], Ch. Voycheva[1]
[1]Faculty of Pharmacy, Medical University of Sofia, Sofia, Bulgaria
[2]Institute of General and Inorganic Chemistry, Bulgarian Academy of Sciences, Sofia, Bulgaria

**Abstract:**

The low water solubility of  bicalutamide (B) is the main obstacle for the satisfactory cytotoxic therapy of prostate cancer. Improvement of the therapeutric effect of bicalutamide into this study is achieved by its incorporation into non-carboxylated (MCN/B) and carboxylated (MCN-COOH/B) mesoporous carbon nanoparticles, chosen because of their high storage capacity, easily-grafted surface, as well as photothermal capacity under near-infrared light (NIR). Carboxylated MCNs exert significant encapsulation efficiency for bicalutamide, slowerer release rate of the active pharmaceutical ingredient (API), as well as higher cytotoxicity against prostate cancer cells, compared to non-carboxylated B-loaded samples. Moreover, the experiments demonstrate that NIR-light provokes faster dissolution speed as well as increased cytotoxicity. This is the reason to consider that the obtained nanosystems could be used as potential drug delivery systems for combined chemo-photothermal therapy of prostate cancer.

**Keywords:** Mesoporous carbon nanoparticles, photothermal effect, bicalutamide, extended release.

## 1.    Introduction

Bicalutamide belongs to the group of nonsteroidal antiandrogen drugs used in the treatment of prostate cancer. Its poor water solubility (BCS class II) leading to unpredictable bioavailability after oral administration is the reason for frequent dosing, side effects and low therapeutic outcomes [1]. A way to overcome these limitations is to include the API into a nanosized drug delivery system which could provide prolonged release of an active substance [1]. Mesoporous carbon nanoparticles (MCN) are promising carriers for cytostatic drugs due to their biocompatibility, high specific surface area, large pore volume and easily-grafted surface [2]. Their internal hydrophobic structure allows high storage capability, especially for aromatic drugs (like bicalutamide) [3,4], while modification of their external surface like carboxylation could increase their dispersion in water [5,6]. Moreover, the presence of strong π-π stacking determines their heat generation capacity - ability to convert the near-infrared light (NIR) into heat to kill cancer cells, which is a prerequisite for application into anticancer photothermal therapy [7-9]. Thus, the MCNs present hydrophobic cavity for high drug loading with opportunity to control the release rate of APIs as well as inherent photothermal effect.

The aim of the present study is to evaluate the applicability of non-carboxylated and carbohylated MCN nanoparticles loaded with bicalutamide for chemo-photothermal therapy.  The cytotoxic potential of non-irradiated and NIR irradiated MCN and MCN-COOH nanoparticles, loaded with bicalutamide in human androgen-sensitive human prostate adenocarcinoma cells was also investigated *in vitro*.

## 2.    Materials and methods

Bicalutamide, sulfuric acid  and sodium lauryl sulphate (SLS) were obtained from MedChemExpress (USB). Empty MCN nanoparticles, ammonium persulphate, acetone, HEPES (anhydrous ≥99.5%), sodium pyruvate, L-glutamine, fetal bovine serum (FBS), RPMI-1640, tripsin/ethylenediaminetetraacetic acid (EDTA), dimethylsulfoxide (DMSO), penicillin and streptomycin were taken from Sigma Aldrich (USA). Androgen-sensitive human prostate adenocarcinoma cells (LNCaP) and Alamar Blue were purchased respectively from Ximbo (UK) and MYBioSource (USA).

### *Carboxylation of MCN*

Functionalization of empty MCNs with carboxylic groups were performed by a one-stage procedure. The preheated MCN (at 120°C for one hour) nanoparticles were incubated into water solution of ammonium

persulfate with sulfuric acid under permanent stirring (180 rpm) and reflux for two hours at 70°C. The procedure continued with centrifugation and drying of the carboxylated MCN nanoparticles (MCN-COOH) in a vacuum desiccator.

### Bicalutamide loading into non-carboxylated and carboxylated MCN

Solvent-impregnation technique was chosen for bicalutamide loading. Preheated at 120ºC for 1 hour MCN and MCN-COOH nanoparticles were incubate into acetone solution of bicalutamide under reflux and permanent stirring (180 rpm) for 24 hours. Water was added as non-solvent and acetone was evaporated by vacuum distillation. Water was removed by centrifugation and the obtained MCN/B and MCN-COOH/B nanoparticles were dried in a vacuum desiccator.

### ATR-FTIR

The possible interactions between the API and the carrier were examined by attenuated total reflection infrared (ATR-FTIR) spectroscopy over the spectral region 400-4000 $cm^{-1}$ with Nicolette 400 (Thermo Fisher Scientific, USA).

### Determination of encapsulation efficiency

Encapsulation efficiency (EE%) for bicalutamide from non-carboxylated nad carboxylated MCN nanoparticles was carried out by calculation of the difference between total amount of the corresponding API used for loading and the amount found in the supernatant (taken immediately after nanoparticles loading). The assay of the API was determined by UV-vis spectrophotometry (Thermo Scientific Evolution 300, USA) under 270 nm ($r^2 > 0.991$).

### Particle size, polydispersity index and zeta potential (DLS analysis)

An average particle size, polydispersity index (PDI) and zeta potential of the empty (carboxylated and non-carboxylated) and loaded with API (MCN/B and MCN-COOH/B) nanoparticles were determined using a Zetasizer Nano ZS (Malvern Instruments, UK).

### In vitro drug release studies

Incubator shaker (Julabo Shake Temp SW23, Germany) was used for the present in vitro drug release studies. The conditions were, as follow: temperature 37°C; shaking rate 100 rpm; media - 50 ml containing 1% water solution of SLS with 10% DMSO (in order to ensure sink conditions for bicalutamide). Pure API and loaded nanoparticles were tasted with or without NIR-irradiation for 3 min. Mean dissolution time (MDT) was used to compare the drug release.

### Cell culture and treatment

LNCaP (androgen-sensitive human prostate adenocarcinoma cells) were obtained from the European Collection of Cell Cultures (ECACC, Salisbury, UK). Cells were cultured in RPMI, supplemented with L-glutamine and fetal bovine serum (FBS) in an incubator, maintaining constant 37ºC, 5% $CO_2$ and maximum humidity. The preparation of the experimental setup included pipetting cell suspension in 96-well plates at $2 \times 10^4$ cells/well. Cells were allowed to attach for 24 h, after which they were treated with either bicalutamide, MCN/B or MCN-COOH/B (bicalutamide concentrations 12.5, 50 and 200 µM).

### NIR irradiation

The plates were irradiated with a NIR lamp (SIL 06, Sanitas, Uttenweiler, Germany) for 5 min, from a distance of 20 cm (adapted from Li *et al.*, 2017). Then, cells were further incubated for 24 h.

### Phase contrast microscopy

The 96-well plates were observed under an inverted phase-contrast microscope to determine the influence of the test substances on monolayer confluency and cell morphology as markers of cell viability. Images were taken at 100x magnification by a Optikam Pro 8LT – 4083, mounted on an inverted Optika XDS-2 microscope (Optika S.r.l., Ponteranica, Italy) in phase contrast mode.

*Cytotoxicity assay*

The contents of the 96-well plates were aspirated and exchanged with a solution of MTT in culture media (final concentration of 5 mg/ml) and incubated for 3 h. Afterwards, the contents of all wells were exchanged with DMSO in order to dissolve the resulting formazan crystals in live cells. After further 30 min of incubation at a place, protected from light, the absorbances in all wells at 570 nm and the reference wavelength of 960 nm was evaluated in a plate reader (Synergy 2, BioTek Instruments, Inc, Highland Park, Winooski, USA). The viability values were expressed as normalized percent values versus the averaged values, obtained from the control group.

*Statistical analyses*

All statistical analyses were done on GraphPad Prism software (version 6, GraphPad Software, La Jolla California USA). The dose response relationships for every treatment group was modelled by non-linear regression and IC50 values were obtained. Cells, treated with different concentrations of MCN/B and MCN-COOH/B were compared via multiple T-tests with Holm-Sidak's correction for multiple testing. The same method was applied to comparing cells, respectively irradiated or not with NIR.

## 3.    Results and discussions

*ATR-FTIR*

The FTIR spectra of bicalutamide, empty and loaded MCN show no shifting of characteristics peaks (data not shown) proving that the API is only physically entrapped into the carriers.

*Encapsulation efficiency, particle size, polydispersity index and zeta potential*

Table 1 summarizes the information about the EE% as well the data from DLS analysis. The Z-potential measurement of all models demonstrates negative values, more pronounced for carboxylated samples as a result of their negative charges. Even though carboxylation leads to increasing of particle size, no agglomeration is observed, evidently from decreasing value of the PDI. The already mentioned internal hydrophobicity of MCN is the reason for the observed high EE% of bicalutamide from non-carboxylated MCN/B (84%) and carboxylated MCN-COOH/B (91%) nanosystems.

|  | MCN | MCN-COOH | MCN/B | MCN-COOH/B |
|---|---|---|---|---|
| **Average size, nm** | 312±8 | 395±8 | 341±7 | 419±5 |
| **PDI** | 0.35 | 0.31 | 0.36 | 0.32 |
| **Z-potential, mV** | -9.02±3 | -34.05±4 | -17.03±2 | -36.13±4 |
| **EE%** | - | - | 84.26%±3 | 92.13%±4 |

Table 1. Particle size, PDI and Z-potential of the empty and loaded MCN-COOH nanoparticles and EE% of bicalutamide for the loaded samples (mean ± SD; n=3)

*In vitro drug release studies*

The dissolution profiles in Figure 1 show extended release of the API from both MCN/B and MCN-COOH/B systems with significantly reduced burst effect for carboxylated nanoparticles compared to dissolution of pure bicalutamide. Dissolution processes from mesoporous carbon systems happen after solvent penetration into the meso-channels, dissolution of API and releasing of dissolved drug. The higher particle size of carboxylated samples compared to non-modified MCN samples gives us the reason to conclude that carboxylation of MCN reflects in slower release rate of bicalutamide. The photothermal conversion capability of MCN nanoparticles is the reason for accelerated drug release from both systems irradiated with NIR light, compared to non-irradiated samples. Such an affect is not observed in the dissolution of pure API. Thus, these NIR-trigger systems could be successfully use to control the exposure of the cancer cells with bicalutamide.
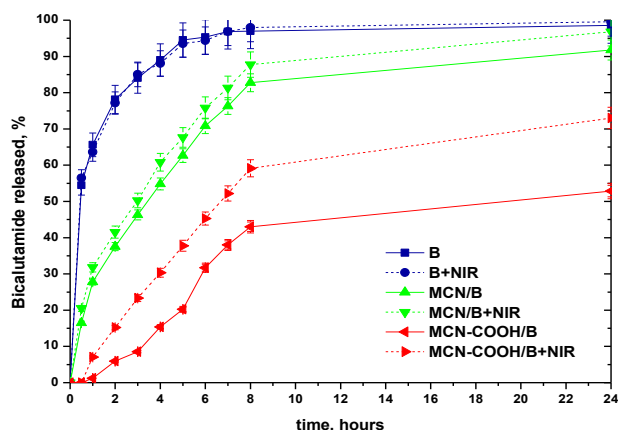
Figure 1. In vitro release profiles of pure bicalutamide (B) and loaded nanoparticle formulations MCN/B and MCN-COOH/B with or without NIR light; mean ± SD; n = 6

### *In vitro cell viability assay*

The aim of the in vitro characterization of MCN particles as bicalutamide drug delivery system were to confirm whether MCN and MCN-COOH retain the pharmacological effects of bicalutamide, whether there are photothermal effects upon acute NIR irradiation and whether –COOH functionalization of MCN influences the aforementioned factors. A dose-response trend is visible after treatment of LNCaP cells with MCN/B and MCN-COOH/B (Figure 2). Carboxylation results in an overall increase in LNCaP cytotoxicity. The differences were statistically significant after treatment with concentrations of both drug-delivery systems, corresponding to 200 µM bicalutamide and upon NIR irradiation – also at the concentration of 50 µM. Furthermore, there was a more pronounced difference between irradiated and non-irradiated groups, when particles were carboxylated, which is especially pronounced in the 200 µM group. Those observations were confirmed by phase-contrast micrographs (data not shown).

### 4. Conclusion

An effective anticancer drug – bicalutamide was physically loaded into non-carboxylated and carboxylated mesoporous carbon nanoparticles with high encapsulation efficiency. The obtained systems exhibit extended release of API, more pronounced and with reduced burst effect for carboxylated samples. Besides this, under NIR light the release of bicalutamide from both MCN/B and MCN-COOH/B systems was accelerated. The enhances cytotoxic activity of carboxilated MCN-COOH/B on LNCaP prostate cancer cells was achieved, most evident with NIR irradiated system, suggesting that the developed system has good potential for effective antitumor therapy. Thus, the obtained mesoporous carbon nanoparticles could be considered as potential drug delivery systems for combined chemo-photothermal therapy of prostate cancer.
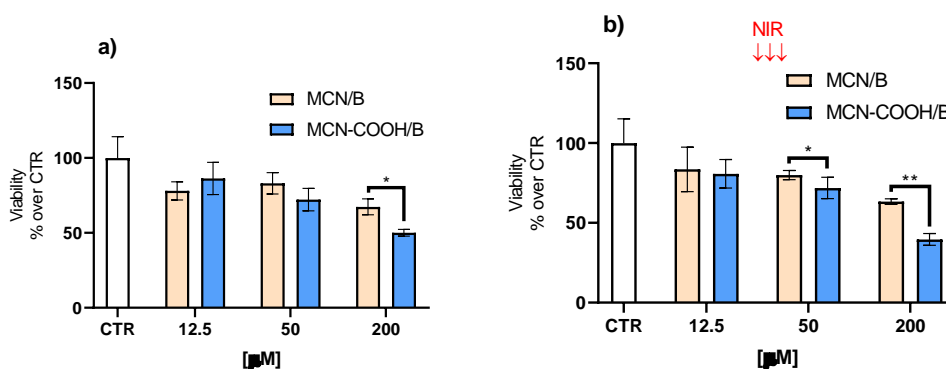


**Figure 2**. Effects of bicalutamide loading in MCN and MCN-COOH particles on the viability of LNCaP cells after 24 h treatment (12.5; 50 or 200 µM bicalutamide) without (a.) or with (b.) irradiation of treated cells with NIR. Multiple T-tests were done, comparing the corresponding MCN/B and MCN-COOH/B groups with Holm-Sidak correction for multiple testing $p* < 0.05$; $p** < 0.01$.

**References:**

1. Guo J., Wu S., Ren W., Wang X., Yang A. Anticancer activity of bicalutamide-loaded PLGA nanoparticles in prostate cancers. Exp. Ther. Med (2015), 10, 2305–2310; DOI: 10.3892/etm.2015.2796.
2. Zhou M., Zhao Q., Wu Y., Feng S., WangD., Zhang Y., Wang S. Mesoporous Carbon Nanoparticles as Multi-functional Carriers for Cancer Therapy Compared with Mesoporous Silica Nanoparticles. AAPS PharmSciTech (2020) 21:42; DOI: 10.1208/s12249-019-1604-8.
3. Gisbert-Garzarán M., Berkmann J., Giasafaki D., Lozano D., Spyrou K., Manzano M., Steriotis T., Duda G., Schmidt-Bleek K., Charalambopoulou G. and Vallet-Regí M. Engineered pH-Responsive Mesoporous Carbon Nanoparticles for Drug Delivery. ACS Applied Materials & Interfaces 2020 12 (13), 14946-14957; DOI: 10.1021/acsami.0c01786.
4. Han C., Huang H, Dong Y., Sui X., Jian B. and Zhu W. A Comparative Study of the Use of Mesoporous Carbon and Mesoporous Silica as Drug Carriers for Oral Delivery of the Water-Insoluble Drug Carvedilol. Molecules (2019), 24, 1770; doi:10.3390/molecules24091770.
5. Huang X., Wu S., Du X. Gated mesoporous carbon nanoparticles as drug delivery system for stimuli-responsive controlled release. Carbon 101 (2016), 135-142; https://doi.org/10.1016/j.carbon.2016.01.094.
6. Hussain A. and Guo S. NIR-triggered release of DOX from sophorolipid-coated mesoporous carbon nanoparticles with the phase-change material 1-tetradecanol to treat MCF-7/ADR cells. J. Mater. Chem. B (2019) 7, 974; DOI: 10.1039/c8tb02673d.
7. Li, X. et al. Hollow mesoporous carbon as a near-infrared absorbing carrier compared with mesoporous carbon nanoparticles for chemo-photothermal therapy. Journal of Colloid and Interface Science (2017) 494, pp. 159–169. https://doi.org/10.1016/j.jcis.2017.01.090.
8. Xu G., Liu S., Niu H., Lva W. and Wu R. Functionalized mesoporous carbon nanoparticles for targeted chemo-photothermal therapy of cancer cells under near-infrared irradiation. RSC Adv. (2014) 4, 33986; DOI: 10.1039/c4ra03993a.
9. Zhou L., Dong K., Chen Z., Ren J., Qu X. Near-infrared absorbing mesoporous carbon nanoparticle as an intelligent drug carrier for dual-triggered synergistic cancer therapy. Carbon (2014), http://dx.doi.org/10.1016/j.carbon.2014.10.091.

# pH-sensitive polymer nanoparticles preparation - a nanoplatform for 5-fluorouracil delivery

Ivelina Ivanova[1], Teodora Popova[1], Marta Slavkova[1], Borislav Tzankov[1], Christina Voycheva[1]
[1] Department of Pharmaceutical Technology, Medical University - Sofia, Bulgaria

**Abstract**

The new polymer was synthesized by grafting acrylic acid (AcA) onto agar agar (AA) backbone. Fourier transform infrared spectroscopy (FTIR), nuclear magnetic resonance (NMR), and differential scanning calorimetry (DSC) were performed to prove the successful grafting and the formation of a new polymer. pH-sensitive nanoparticles, prepared by using glutaraldehyde (GA) as a crosslinker, were loaded with 5-fluorouracil (5-FU). The resulting nanoparticles were characterized by transmission electron microscopy (TEM), and dynamic light scattering (DLS). Drug loading efficiency (DLE), and drug release were also determined.

**Keywords:** pH-sensitivity, nanoparticles, 5-Fluorouracil, grafting

## 1. Introduction

5-Fluorouracil is an antimetabolite used to treat colorectal, stomach, breast, pancreas, ovary, liver, and other solid tumors [1–3]. The major drawback of 5-FU is that the appearance of drug resistance is a significant limitation of its clinical usage, leading to high toxicity and side effects such as gastrointestinal, hematological, neural dermatological, myelosuppression, and cardiotoxicity [4,5]. Polymeric nanoparticles' small size (below 1000 nm) and variable morphologies could affect 5-FU efficacy by increasing circulation time, reducing side effects, and improving its therapeutic index. [6,7]. Moreover, they have the potential to penetrate through the cells and tissue, to arrive at target organs, and to pass through the smallest capillary vessels, avoiding rapid clearance by phagocytes, thereby prolonging their stay in the bloodstream. The controlled release that they can afford could reduce the toxicity of loaded drugs [6]. The development of stimuli-sensitive multi-particulate formulation is a promising platform for sustained release and drug targeting [9,10]. Based on their physicochemical properties, polymers could respond to different stimuli, like pH, temperature, light, magnetic field, enzymes, ionic strength, ultrasound, and redox change [11]. Their functional groups allow them to be grafted or crosslinked with synthetic polymers obtaining stimuli-sensitive behavior [12]. The graft polymers are usually obtained by use of initiators or by gamma rays, UV, or microwave radiation to create the free radical site on the polymer chain. Monomeric units are attached like a side chain to a polymer backbone to form a branched polymer with desirable properties different from the base polymer [13]. pH or proton concentration is an interest-provoked stimulus because of anatomical and pathological differences in the human body. A well-known fact is that the gastrointestinal tract has pH-varying media from 1 to 7.5. The neoplastic cells are characterized by lower intercellular pH (pH≈4-5) [14] and extratumoral pH 7.4. pH-sensitive polymers are polyelectrolytes with ionizable groups whose solubility in aqueous solution is influenced by environmental pH. In this study, we grafted acrylic and methacrylic acid units to an agar backbone to achieve the pH sensitivity of the resulting polymer. To achieve an enhanced permeability and retention effect in the tumor tissue from the resulted pH sensitive polymer the nano-range particles we obtained, then loaded with 5-fluorouracil.

## 2. Materials and methods

AA, AcA, Ammonium ceric nitrate (CAN), Nitric acid (HNO$_3$), and GA were purchased from Sigma-Aldrich. Hydroquinone (HQ) was purchased from TCI America. Deionized water was prepared in the laboratory.

Preparation of agar agar-g-polyacrylic acid (AA-g-AcA).

Agar was dissolved in distilled water at 90°C in a three-neck round bottom flask with a gas inlet system and a condenser followed by the addition of acrylic under stirring. Nitrogen gas was poured for 60 minutes. A solution of CAN in water, acidified with concentrated HNO$_3$ was added. The reaction continued in a thermostatic paraffin bath under stirring for 6 h at a constant temperature of 70°C. The grafting procedure terminated by adding a saturated HQ solution when a separating funnel splits the resulting polymer AA-g-AcA from the homopolymer. Finally, the graft copolymer hydrogel was precipitated over acetone, separated by centrifugation, dried to a constant weight, and grounded.

The ratio between polymer, monomer, and initiator is shown in Table 1.

Table 1: Polymer, monomer, and initiator ratios used for the model grafted polymer and formulation parameters and characterization of the AA-g-AcA nanoparticles.

| Code | Wt.of agar (g) | Wt. of AcA (g) | Wt of CAN (g) | Polymer | Drug/polymer ratio (w/w) | GA (ml) | DLE% |
|---|---|---|---|---|---|---|---|
| Agar (AA) | - | - | | AA-g-AcA | 1/1 | 2 | 20.81 ± 2.80 |
| AA-g-AcA1 | 1 | 10 | 0.1 | | 1/1 | 3 | 32.66 ± 1.52 |
| AA-gAcA2 | 1 | 10 | 0.2 | | 1/1 | 4 | 39.12 ± 2.72 |
| AA-g-AcA3 | 1 | 10 | 0.3 | AA-g-AcA | 1/2 | 2 | 35.25 ± 1.42 |
| AA-gAcA4 | 1 | 5 | 0.2 | | 1/2 | 3 | 56.86 ± 0.03 |
| AA-g-AcA5 | 1 | 15 | 0.2 | | 1/2 | 4 | 62.44 ± 2.40 |
| | | | | AA-g-AcA | 1/3 | 2 | 53.33 ± 2.17 |
| | | | | | 1/3 | 3 | 72.90 ± 1.69 |
| | | | | | 1/3 | 4 | 78.42 ± 1.19 |

Preparation of empty and loaded with 5-FU nanoparticles.

The empty and loaded with 5-FU nanoparticles AA-g-AcA were prepared according to the modified protocol [15]. The polymer was placed in distilled water or a solution of 5-FU and stirred to form a homogenous solution for 2 h, then added by spraying into a stirred water containing GA (crosslinker) and $HNO_3$ (catalyst) using a spraying device under ultrasound for 4 min (0.04 wats). The formed nanoparticles were then removed from the crosslinking solution by centrifugation and washed with water repeatedly to remove the glutaraldehyde and acid residue. Finally, the nanoparticles were completely dried under a vacuum at 40°C. The ratio between polymer, monomer, and crosslinker is shown in Table 1. The resulting nanoparticles were named as follows: empty nanoparticles AA-g-AcA (npAA-g-AcA), loaded nanoparticles AA-g-AcA (npAA-g-AcA/5-FU).

***Nuclear magnetic resonance***, ***Transform Infrared Spectroscopy, Differential Scanning Calorimetry***, ***Transmission electron micrograph***, ***Dynamic Light Scattering***
***Drug loading efficiency***

The percent of loading efficiency was calculated according to the following equation:

$$\text{Drug Loading Efficiency \% (DLE\%)} = \frac{5-\text{FU total} - 5-\text{FU filtrate}}{5-\text{FU total}} \times 100 \tag{1}$$

***In vitro drug release study***

The in vitro drug release from the nanoparticles was studied in phosphate buffers (pH 7.4 and 5). A medium with pH 5 was chosen to simulate the environmental conditions in tumor cells [14]. The freshly prepared nanoparticle dispersion was introduced into a dialysis membrane bag (MW = 6000–8000), placed into 40 ml of release medium, and incubated in a shaking water bath at 37°C under a 100 rpm. At appropriate time intervals, an aliquot sample was withdrawn, the amount of 5-FU released from the nanoparticles was evaluated by a UV spectrophotometer at a λmax of 270 nm, and the aliquot release medium was compensated with a fresh one.

## 3. Results and discussion

***NMR*** When the acrylic acid was grafted on AA, the peak at 3.96 ppm in the spectra of AA showed decreased signal strength as monomer moieties replaced the hydroxyl group. The AcA carboxylic group's proton peak shifted to 12.16 ppm. Compared with the spectrum of AA, in the spectrum of AA-g-AcA new proton signals appeared at 1.5 ppm, 1.7 ppm, and 2.2 ppm for- –OH and methylene protons of AcA, respectively. These results demonstrated the formation of AA-g-AcA.

***DSC*** The peak of 211°C was new and corresponded to the melting points of AA-g-AcA. It is assigned by the formation of the new polymeric structure by the combination of AA and AcA. The grafted polymer thermal profiles demonstrated the presence of agar on their structure and the obtention of new polymeric material. Additionally, the AA-g-AcA exhibited an enhancement in thermal resistance compared to agar since no exothermic signal was observed.

***FTIR*** spectra were used as a prove for the successful grafting of AA-g-AcA. The difference between the monomer and the grafted polymer spectra is the absence of a signal at 1634 cm$^{-1}$ for the vinyl group of AcA. The absence of the stretching vibrations found in the AA spectrum of $CH_2OH$ at 1033 cm$^{-1}$ in spectra of grafted

polymers proved the successful grafting of monomer units onto the AA backbone. No changes in the main peaks in IR spectra of npAA-g-AcA/5-FU were observed, so physical incorporation of 5-FU in both types of nanoparticles could be assumed.

***TEM*** studies were performed for analysis of the size, shape, and structure of AA-g-AcA and AA-g-AcA/5-FU nanoparticles (Fig.1 ).
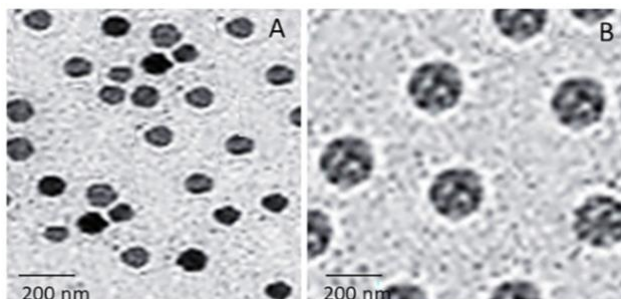


**Fig. 1**: TEM of (A) npAA-g-AcA, npAA-g-AcA/5-FU

As seen, empty nanoparticles show spherical shape, nanoscale size, matrix structure, and narrow distribution. The same shape, structure, and distribution are observed for the loaded nanoparticles. The increase in size after loading is visible.

***DLS*** Measurements performed by DLS analysis show particle size in the nano range for obtained particles. The nanoparticle diameter for both polymers increased with the loading of the drug. Probably the entrapment of the drug in the free volume areas of the polymer particles prevents the additional shrinking.

**Table 2:**     Average size, polydispersity index (PDI), and zeta potential results from DLS analysis

| Parameter | AA-g-AcA empty | AA-g-AcA /5-FU |
|---|---|---|
| Size, nm | 124.7±7.3 | 250±8.4 |
| PDI | 0.38 | 0.27 |
| Zeta potential, mV | - 20.1±3.7 | -33.6±3.6 |

The PDI value proved the stability of empty particles and narrow limits in size distribution. With the 5-FU loading, the polydispersity index for polymer particles decreases, most probably due to the change in the zeta potential value. 5-FU (pKa=8.0) is negatively charged in physiological conditions. After loading, negatively charged due to carboxyl groups' presence, empty polymer particles accumulate the drug's negative charge, reflecting on the zeta potential value.

### *Drug loading efficiency*

Nanoparticles were prepared in different drug/polymer ratios and crosslinker amounts, and the data are presented in Table 1. Increasing the amount of polymer in the drug/polymer ratio results in the retention of a greater amount of 5-FU in the particles. This is probably a result of increased hydrogen bonds that the drug and the polymer create between themselves because of the larger number of hydroxyl groups on the polymer's side. The drug loading efficiency decreases with an increase in the amount of drug used during the preparation of the nanoparticles. Maximum DLE was found at a drug/polymer ratio of 1/3. The exceeding amount of 5-FU above the maximum loading efficiency is probably washed after the lavation of the obtained particles because of the drug's good water solubility. However, increasing the amount of GA leads to an increase in the DLE value, most likely due to the tighter crosslinking, which allows a greater amount of 5-FU to be retained.

Based on the drug loading efficiency calculations results, the experiments continued with the nanoparticles prepared with a drug/polymer ratio of 1/3 and a 4 ml crosslinker.

### *In vitro drug release study*

The pH-dependent release of 5-FU was observed by performing an in vitro dissolution test in pH 7.4 and 5.0 buffer media at 37°C. The results are presented in the figure. At pH 7.4, the nanoparticles showed a sustained release about 20% in 72 h. This delay is probably due to the swelling of the polymer under these conditions (data not shown). Swelling significantly slows the release of API due to the additional crosslinking of the

polymer that occurs during the process of preparation of the nanoparticles. The obtained gel layer slowed down the release of 5-FU.

At pH 5.0, npAA-g-AcA/5-FU show increased and faster release. Such pH conditions are associated with the tumor cells because of their extensive metabolism [14]. Moreover, the obtained nanoparticles at the simulated tumor conditions show an initial burst effect for the first 6 h. A gradual, controlled release and 100% from npAA-g-AcA were observed over time at 24 h. This faster release is associated with polymers' swelling behavior, used for nanoparticle preparation and physical entrapment of 5-FU in the polymer nanoparticles. At pH 5 polymer swell to a lower extent, which allows faster API release. The slower release of 5-FU at physiological pH (pH=7.4) is an advantage as it may reduce drug loss until it reaches the target tumor tissue which is a prerequisite for lowering systemic toxicity. In the bloodstream, as the particles pass from a pH 7.4 region to a pH 5.0 region, the release would be promoted due to the contraction of the polymer chains and the release of API located in the voids of the swollen polymer at pH 7.4.

## 4. Conclusion

In the present study, the grafting of AcA onto agar was carried out by free radical polymerization using CAN as an initiator to prepare 5-FU loaded nanoparticles after crosslinking with GA. The results demonstrated that the drug release depends on the pH of the medium. 5-FU released from AA-g-AcA nanoparticles is extended to 48h.

## Funding

## References

1.  N. Zhang, Y. Yin, S.-J. Xu, W.-S. Chen, 5-Fluorouracil: mechanisms of resistance and reversal strategies, Mol. Basel Switz. 13 (2008) 1551–1569. https://doi.org/10.3390/molecules13081551.
2.  J.A. Meyerhardt, R.J. Mayer, Systemic therapy for colorectal cancer, N. Engl. J. Med. 352 (2005) 476–487. https://doi.org/10.1056/NEJMra040958.
3.  D.B. Longley, D.P. Harkin, P.G. Johnston, 5-fluorouracil: mechanisms of action and clinical strategies, Nat. Rev. Cancer. 3 (2003) 330–338. https://doi.org/10.1038/nrc1074.
4.  F. Farjadian, A. Ghasemi, O. Gohari, A. Roointan, M. Karimi, M.R. Hamblin, Nanopharmaceuticals and nanomedicines currently on the market: challenges and opportunities, Nanomed. 14 (2019) 93–126. https://doi.org/10.2217/nnm-2018-0120.
5.  Y.S.R. Krishnaiah, V. Satyanarayana, B. Dinesh Kumar, R.S. Karthikeyan, P. Bhaskar, In vivo pharmacokinetics in human volunteers: oral administered guar gum-based colon-targeted 5-fluorouracil tablets, Eur. J. Pharm. Sci. Off. J. Eur. Fed. Pharm. Sci. 19 (2003) 355–362. https://doi.org/10.1016/s0928-0987(03)00139-
6.  T. Jung, W. Kamm, A. Breitenbach, E. Kaiserling, J. Xiao, T. Kissel, Biodegradable nanoparticles for oral delivery of peptides: Is there a role for polymers to affect mucosal uptake, Eur. J. Pharm. Biopharm. Off. J. Arbeitsgemeinschaft Für Pharm. Verfahrenstechnik EV. 50 (2000) 147–60. https://doi.org/10.1016/S0939-6411(00)00084-9.
7.  C.P. Reis, R.J. Neufeld, A.J. Ribeiro, F. Veiga, Nanoencapsulation I. Methods for preparation of drug-loaded polymeric nanoparticles, Nanomedicine Nanotechnol. Biol. Med. 2 (2006) 8–21. https://doi.org/10.1016/j.nano.2005.12.003.
8.  S. Siraj, P. Sudhakar, U.S. Rao, K.V. Sekharnath, K.C. Rao, M.C.S. Subha, INTERPENETRATING POLYMER NETWORK MICROSPHERES OF POLY (VINYL ALCOHOL)/METHYL CELLULOSE FOR CONTROLLED RELEASE STUDIES OF 6-THIOGUANINE, Int. J. Pharm. Pharm. Sci. (2014) 101–106.
9.  N.S. Rejinold, K.P. Chennazhi, S.V. Nair, H. Tamura, R. Jayakumar, Biodegradable and thermo-sensitive chitosan-g-poly(N-vinylcaprolactam) nanoparticles as a 5-fluorouracil carrier, Carbohydr. Polym. 83 (2011) 776–786. https://doi.org/10.1016/j.carbpol.2010.08.052.
10. N. Avramović, B. Mandić, A. Savić-Radojević, T. Simić, Polymeric Nanocarriers of Drug Delivery Systems in Cancer Therapy, Pharmaceutics. 12 (2020) 298. https://doi.org/10.3390/pharmaceutics12040298.
11. S. Durkut, Y.M. Elçin, Synthesis and characterization of thermosensitive poly(N-vinylcaprolactam)-g-collagen, Artif. Cells Nanomedicine Biotechnol. 45 (2017) 1665–1674. https://doi.org/10.1080/21691401.2016.1276925.
12. Polymer Grafting and Crosslinking | Wiley, Wiley.Com. (n.d.). https://www.wiley.com/en-es/Polymer+Grafting+and+Crosslinking-p-9780470404652 (accessed August 13, 2023).
13. P. Bawa, V. Pillay, Y.E. Choonara, L.C. du Toit, Stimuli-responsive polymers and their applications in drug delivery, Biomed. Mater. Bristol Engl. 4 (2009) 022001. https://doi.org/10.1088/1748-6041/4/2/022001.

14. M. Maghsoudi, M. Abbasian, K. Farhadi, F. Mahmoodzadeh, M. Ghorbani, M. Hoseinzadeh, Mesoporous Si-MCM-41/Polymer as a pH-Responsive Drug Delivery System for Cancer Therapy, ChemistrySelect. 5 (2020) 11901–11909. https://doi.org/10.1002/slct.202002071.

15. P. Bawa, V. Pillay, Y.E. Choonara, L.C. du Toit, Stimuli-responsive polymers and their applications in drug delivery, Biomed. Mater. Bristol Engl. 4 (2009) 022001. https://doi.org/10.1088/1748-6041/4/2/022001.

# Nonlinear Optical Properties of Two-Dimensional Materials – A Study on their Suitability for Laser Protection Applications

Stefanie Dengler[1], Michael Henrichsen[1]

[1]Fraunhofer IOSB, Gutleuthausstr. 1, 76275 Ettlingen, Germany, stefanie.dengler@iosb.fraunhofer.de

**Abstract**

In recent years, two-dimensional layered materials, especially graphene and graphene oxide have received significant attention due to their unique properties and potential applications in various fields. Graphene materials have also attracted interest in the field of optical limiting due to their excellent nonlinear optical properties. In this work a comprehensive study on the nonlinear optical response of dispersed graphene oxide, boron nitride nanosheets, molybdenum disulfide nanosheets and tungsten disulfide nanosheets is presented. In addition, nanohybrids were generated by functionalizing of the nanosheets with zinc tetraphenylporphyrin. Their optical limiting behaviour is characterised by means of nonlinear transmittance and scattered energy measurements. Our results show that nonlinear scattering dominates the optical limiting performance of all measured nanomaterials.

**Keywords:** 2D materials, optical limiting, nonlinear absorption, nonlinear scattering

## 1. Introduction

The demand for efficient protection of the human eye and sensitive devices and optics from laser radiation is constantly growing due to the increasing use of lasers with different wavelengths in all areas of life.

One potential method of protection can be realized by using nonlinear optical (NLO) materials, provided that they possess the ability to limit the transmitted energy. The so-called optical limiting (OL) is a NLO process where material properties change with increasing energy density of laser radiation in such a way that the transmitted energy density remains almost constant over a wide range of irradiated power (Fig. 1). Hence, a linear relationship between input and output energy exists only at energies below a threshold.
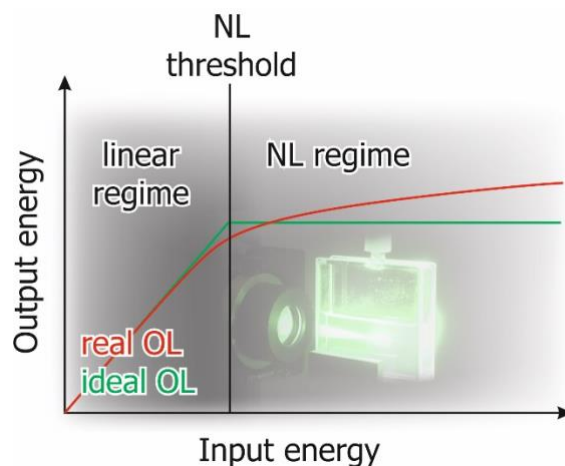


**Fig. 1**: Schematic drawing illustrating ideal and real optical limiting performance.

There are two ways to reduce the intensity of laser radiation when using OL devices for laser protection. Either a part of the laser beam is absorbed or it is distributed over a larger area. A variety of NLO effects can trigger OL behaviour, the most important effects are nonlinear (NL) absorption, NL scattering and NL refraction [**Error! Reference source not found.**]. Currently, there are no materials that fully satisfy the requirements for optical limiting applications, particularly for eye protection. The ideal material should have a low threshold, provide sufficient attenuation and be efficient across a broad range of wavelengths. Therefore, research is ongoing to find new materials with an improved optical limiting efficiency and to enhance the properties of established optical limiting materials. In recent years, two-dimensional materials, especially graphene and graphene oxide have received significant attention due to their unique optical properties and potential applications in various fields, including optical limiting [2, 3].

In this work a comprehensive study on the nonlinear optical response of dispersed graphene oxide (GO NS), boron nitride nanosheets (BN NS), molybdenum disulfide nanosheets ($MoS_2$ NS) and tungsten disulfide nanosheets ($WS_2$ NS) is presented. Additionally, nanohybrids were generated by functionalizing the nanosheets with zinc tetraphenylporphyrin (ZnTPP). The optical limiting behaviour is characterized by means of nonlinear transmittance and scattered energy measurements using nanosecond laser pulses at 532 nm.

## 2. Experimental

### 2.1. Sample Preparation

Different ethanol/water mixtures were used to generate dispersions, since pure water and pure ethanol can hardly disperse the nanosheets, except GO. $MoS_2$ NS was dispersed in 45 vol% water and 55 vol% ethanol, $WS_2$ NS in 35 vol% water and 65 vol% ethanol, BN NS in 55 vol% water and 45 vol% ethanol and GO NS in pure water. All samples were sonicated for 6 hours in an ultrasonic bath. The dispersions, prepared with the aforementioned methodology, exhibited high stability and did not precipitate. To investigate their OL properties the concentration of all samples was adjusted to have around the same transmittance at the used laser wavelength of 532 nm.

In addition, nanohybrids were prepared by anchoring the OL dye ZnTPP to the nanosheets. A drop of ZnTPP solution was added to the dispersions and was also measured after stayed overnight.

### 2.2. Experimental Setup

The experimental setup to measure the NLO response is described in detail in a previous publication [4]. A drawing of the setup used for the OL studies is shown in Fig. 2. In brief, a frequency-double Nd:YAG laser system (Coherent Infinity), operating at a wavelength of 532 nm and a 1 Hz pulse repetition rate with a pulse length of approximately 3 ns was employed. A beam splitter was used to divide the beam into a reference beam and a signal beam. The reference beam was used to determine the energy of the laser pulses (detector D1). The samples were placed in the intermediate focal plane of a f/5 Keplerian telescope formed by the lenses L1 and L2 (focal lengths 60 mm and 100 mm) in Fig. 2. The diameter of the laser focus was measured by the knife-edge method to be 5 µm at a wavelength of 532 nm. The focusable energy (or encircled energy), which is generally defined as the energy detected within a solid angle of 1.5 mrad, was measured using lens L3 (focal length 400 mm) and pinhole A3 (diameter 600 µm) in front of the signal photodiode D3. The portion of scattered radiation at 30° in the forward direction was recorded simultaneously with the assistance of detector D2.
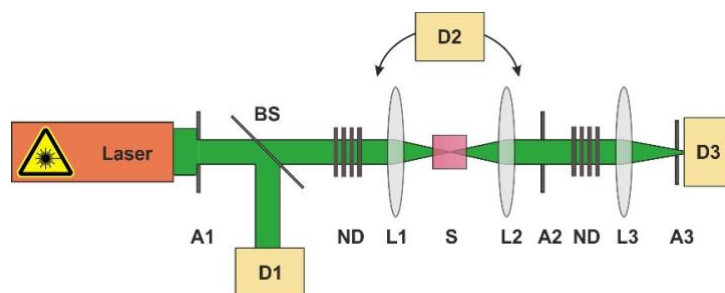


**Fig. 2**: Experimental setup to study NL transmittance and scattering. With L1, L2, and L3 - lenses; S - sample; D1, D2 and D3 - photodiodes; BS - beamsplitter; A1, A2, and A3 - apertures.

## 3.    Results and Discussion

The OL properties were investigated using nanosecond (~3 ns) laser pulses at 532 nm. In order to assess the potential of the nanosheet dispersions for OL applications the results were compared with GO NS. GO dispersions are well known for their suitability as optical limiters at 532 nm. Their OL performance has been extensively studied during the last years and it is generally believed that NL scattering dominates their NLO properties [2, 5].
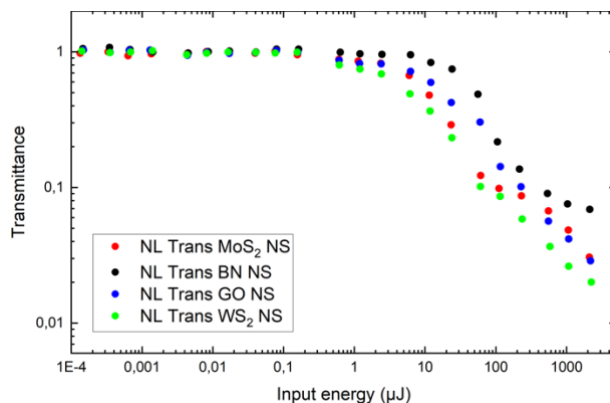


**Fig. 3**: Normalised NL transmittance of $MoS_2$ NS, BN NS, GO NS and $WS_2$ NS dispersions.

The normalised NL transmittance and NL scattering at 30°, plotted as a function of the incident pulse energy, is shown in Fig. 3. The input energy was varied from 0.1 nJ up to 2 mJ. At low input energies, the transmittance is independent of the irradiated energy. With further increasing input energy, after the material-specific OL threshold, the transmittance becomes intensity-dependent and decreases. The transmittance begins to decrease at approximately 0.5 µJ for $MoS_2$ NS, GO NS and $WS_2$ NS and at approximately 6 µJ for BN NS. The overall highest NL attenuation with almost two orders of magnitude at a laser energy of 2 mJ is achieved by $WS_2$ NS. The NL attenuation of GO NS and $MoS_2$ NS are comparable at high laser energies, whereas the NL attenuation in the intermediate regime of $MoS_2$ is a slightly higher. BN NS exhibits the lowest NL attenuation.

The NL transmittance and scattering of all samples and their respective hybrids is displayed in Fig. 4. In the case of BN NS, the addition of ZnTPP results in enhanced OL performance, however, it remains inferior to the other samples. The anchoring of ZnTPP to GO NS also results in a reduction of the NL threshold and an increase in attenuation. The addition of ZnTPP to $MoS_2$ NS does not change its OL behaviour, as the NL threshold as well as the NL attenuation remain the same. The OL parameters (NL threshold and NL attenuation at maximum input energy of 2 mJ) of all samples are presented in Table 1 for reference. All samples display relevant NL scattering, comparable to that observed in GO NS or even stronger, which suggests that NL scattering is the primary OL mechanism in all measured samples.

Table 1: Optical limiting parameters (NL threshold and NL attenuation at maximum input energy of 2 mJ) of all samples.

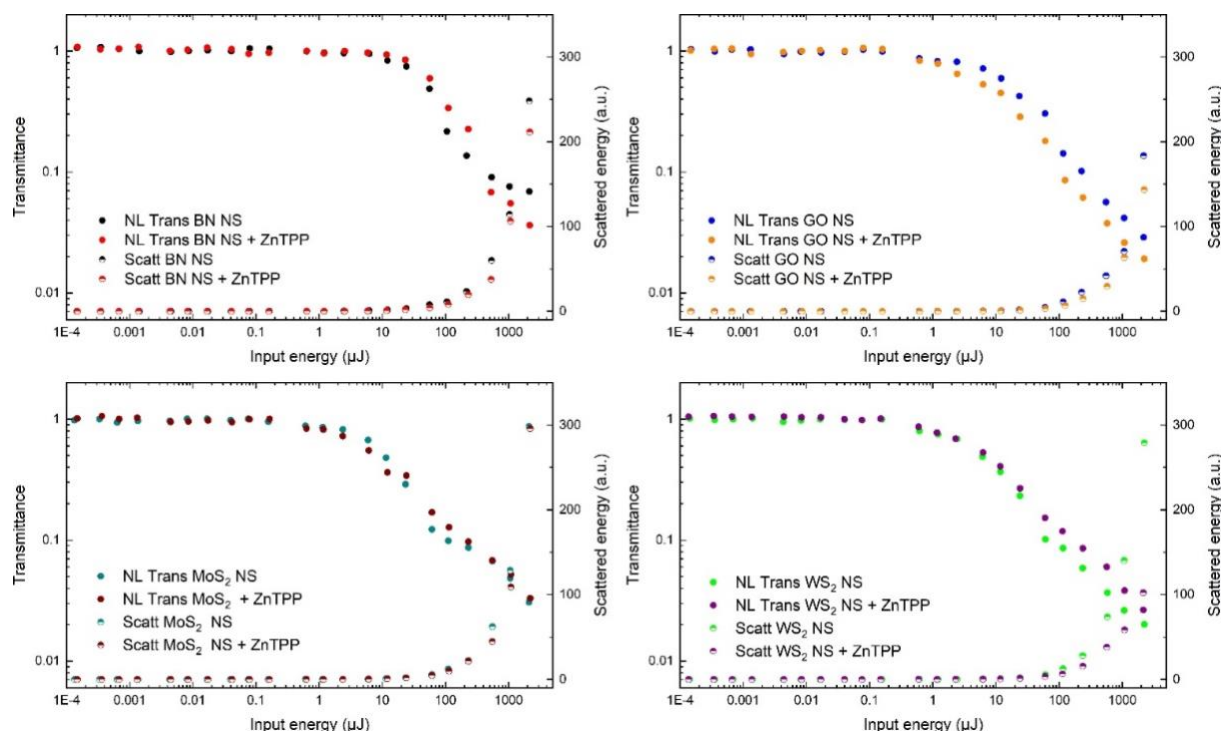| Sample | NL threshold (µJ) | NL attenuation (OD) @ $E_{in}$(max) |
|---|---|---|
| $MoS_2$ NS | 0.6 | 1.50 |
| $MoS_2$ NS + ZnTPP | 0.6 | 1.51 |
| GO NS | 0.6 | 1.54 |
| GO NS + ZnTPP | 0.6 | 1.72 |
| $WS_2$ NS | 0.5 | 1.71 |
| $WS_2$ NS + ZnTPP | 0.5 | 1.58 |
| BN NS | 6 | 1.18 |
| BN NS + ZnTPP | 12 | 1.44 |

Fig. 4: Normalised NL transmittance and scattering at 30° in forward direction as a function of the incident pulse energy for the dispersions of BN NS and BN NS + ZnTPP (top left), GO NS and GO NS + ZnTPP (top right), MoS$_2$ NS and MoS$_2$ NS + ZnTPP (bottom left) and WS$_2$ NS and WS$_2$ NS + ZnTPP (bottom right).

## 4. Conclusion

The optical limiting properties of dispersed graphene oxide, boron nitride nanosheets, molybdenum disulfide nanosheets and tungsten disulfide nanosheets were investigated. Furthermore, nanohybrids were generated by functionalising of the nanosheets with zinc tetraphenylporphyrin. The most effective optical limiting performance with the highest nonlinear attenuation was observed in the case of tungsten disulfide nanosheets. In case of graphene oxide, the optical limiting properties could be enhanced through the addition of zinc tetraphenylporphyrin, resulting in a performance that was comparable to that of tungsten disulphide nanosheets. Tungsten disulfide nanosheets and functionalised graphene oxide have been identified as two promising candidates for laser protection applications due to their large optical limiting effect.

## References

1. S. Dengler and B. Eberle, "Investigations on the Nonlinear Optical Properties of 0D, 1D, and 2D Boron Nitride Nanomaterials in the Visible Spectral Region," *Nanomaterials*, vol. 13, 1849, 2023
2. M. Feng, H. Zhan and Y. Chen, "Nonlinear optical and optical limiting properties of graphene families," Appl. *Phys. Lett.*, vol. 96, 033107, 2010
3. Y. Wang, Y. Wang, K. Chun, K. Qi, T. Xue, H. Zhang, J. He and S. Xiao, "Niobium carbide MXenes with broad-band nonlinear optical response and ultrafast carrier dynamics," ACS Nano, 14, 10492–10502, 2020
4. G.Ritt, S. Dengler and B. Eberle, "Protection of optical systems against laser radiation", *Proc. SPIE, Electro-Optical and Infrared Systems: Technology and Applications VI*, Berlin, Germany, 2009, vol. 7481, 74810U
5. B. Wang, Y. Hernandez, M. Lotya, J. N. Coleman and W. J. Blau, "Broadband Nonlinear Optical Response of Graphene Dispersion," Adv. Mater. 21, 2430–2435, 2009